

Hyperpolarised Carbon-13 Magnetic Resonance Spectroscopy with [1-^{13}C]Ethylpyruvate as a Preclinical Modality for Detecting MS-Like Lesions and their Response to Fingolimod Treatment in the Focal Experimental Autoimmune Encephalomyelitis Rat Model of Multiple Sclerosis

Dr Richard Healicon

Linacre College, University of Oxford

Dissertation submitted for the degree of MSc(Res) Physiology, Anatomy and Genetics

Contents

Acknowledgements....6

Abstract....7

Chapter 1 – Introductory Information....8

1.1 Introduction to Magnetic Resonance Imaging and Spectroscopy....8

1.1.1 Proton Magnetic Resonance Imaging....8

1.1.2 Proton Spectroscopy....11

1.1.3 Dynamic Nuclear Polarisation....12

1.1.4 Hyperpolarised ^{13}C Magnetic Resonance Spectroscopy....13

1.1.5 Pyruvate and Ethylpyruvate in Metabolism....14

1.1.6 [1-^{13}C]Ethylpyruvate vs. [1-^{13}C]Pyruvate as a Hyperpolarised ^{13}C MRS Tracer Molecule for Neuroimaging....16

1.2 Multiple Sclerosis....17

1.3 Pathogenesis and Pathophysiology of Multiple Sclerosis....19

1.3.1 Predisposition and Susceptibility to Multiple Sclerosis....19

1.3.2 Pathogenesis of Multiple Sclerosis....20

1.4 Diagnosis of Multiple Sclerosis....26

1.5 Multiple Sclerosis Treatments....30

1.6 Animal Models of Multiple Sclerosis....32

1.6.1 Experimental Autoimmune Encephalomyelitis....33

1.6.2 Viral Multiple Sclerosis Models....34

1.6.3 Toxic Multiple Sclerosis Models....35

1.6.4 Focal Experimental Autoimmune Encephalomyelitis....35

Summary of Chapters 37

Chapter 2 – Optimising an [1-^{13}C]Ethylpyruvate Mixture for DNP.....38

2.1 Introduction.....38

2.2 Methods.....39

2.2.1 Overview.....39

2.2.2 [1-^{13}C]Ethylpyruvate-Finland Radical Sample Preparation 39

2.2.3 [1-^{13}C]Ethylpyruvate-AH111501 Radical Sample Preparation.....40

2.2.4 [1-^{13}C]Ethylpyruvate Hyperpolarisation.....40

2.2.5 Data Fitting and Statistical Analysis.....41

2.3 Results.....42

2.4 Discussion.....44

Chapter 3 – Optimising an Anaesthetic Protocol for Hyperpolarised ^{13}C Neuroimaging.....46

3.1 Cerebral Oxygen Consumption and Perfusion 46

3.2 Methods.....49

3.2.1 Overview.....49

3.2.2 Animal Handling.....49

3.2.3 Anaesthetic Protocol.....50

3.2.4 [1-^{13}C]Pyruvate MRS.....50

3.2.5 Perfusion Weighted MRI.....51

3.2.6 [1-^{13}C]Pyruvate MRS Processing 51

3.2.7 DSC MRI Processing.....52

3.2.8 Statistical Analysis.....52

3.3 Results.....52

3.3.1 Perfusion MRI....52
3.3.2 Hyperpolarised [1-^{13}C]Pyruvate MRS....54
3.4 Discussion....58
3.4.1 Hyperoxia Reduces Cerebral Perfusion....58
3.4.2 Hyperoxia and Baseline Cerebral Metabolism....60
3.4.3 Conclusion....63
Chapter 4 – Hyperpolarised [1-^{13}C]Ethylpyruvate MRS as a Tool to Investigate Metabolism and Treatment Response to Fingolimod in fEAE Rats....64
4.1 Metabolic Changes in Immune and Brain Cells in Inflammation....64
4.1.1 Immune Cell Metabolism....64
4.1.2 Cerebral Metabolism....66
4.1.3 [1-^{13}C]Ethylpyruvate as a Tracer for Neuroinflammation....69
4.2 Methods....70
4.2.1 Overview....70
4.2.2 Animal Handling and Anaesthesia....70
4.2.3 fEAE Lesion Generation and Treatment with Fingolimod....70
4.2.4 [1-^{13}C]Ethylpyruvate MRS and Analysis....71
4.2.5 Proton MRI....72
4.2.6 Histology....72
4.2.7 Statistical Analysis....73
4.3 Results....73
4.3.1 Hyperpolarised [1-^{13}C]Ethylpyruvate MRS....73
4.3.2 Proton MRI....75

4.3.3 Histology 75

4.4 Discussion 76

4.4.1 Confirmation of Lesion Development 76

4.4.2 Lesion Detection and Treatment Response with [1-^{13}C]Ethylpyruvate MRS 78

4.4.3 Conclusions 79

Chapter 5 – Closing Comments 82

Bibliography 85

Acknowledgements

I would like to thank Dr James Grist for his support and help in all aspects of this project, and particularly for his patience in explaining physics and coding to a medic. I would like to thank Professor Damian Tyler for overseeing my work and for his excellent feedback, Vicky Ball for all her help, advice and teaching during my time in the lab, and Professor Daniel Anthony for providing us with the technical skills and knowledge to establish our experimental model and perform our histological analysis.

Abstract

Multiple sclerosis (MS) is a demyelinating, immune-mediated disease of the central nervous system characterised by both acute episodes of neurological dysfunction and long-term neurodegeneration.

Diagnosis and monitoring rely heavily on imaging, with magnetic resonance imaging (MRI) the present gold-standard modality. Current MRI techniques, however, have poor sensitivity for monitoring the development of pre-demyelinated lesions and in assessing treatment response.

In MS lesions, highly active immune cells and dysregulated neuronal metabolism cause a localised metabolic shift towards glycolytic lactate production. Hyperpolarised ^{13}C magnetic resonance spectroscopy (MRS) is able to detect this shift, and here, I have demonstrated the ability of hyperpolarised [1-^{13}C]ethylpyruvate MRS to detect MS-like lesions, and their response to fingolimod treatment, in the focal experimental autoimmune encephalomyelitis rat model of MS. This paves the way for future studies using hyperpolarised [1-^{13}C]ethylpyruvate MR in rodent models of MS, and eventually in patients with MS.

In hyperpolarised MR, high levels of signal are generated in ^{13}C-labelled tracer molecules using the process of dynamic nuclear polarisation. This requires the tracer molecule to be mixed with a free radical, which facilitates transfer of electron polarisation to the tracer molecule. To optimise an experimental protocol for this and future hyperpolarised [1-^{13}C]ethylpyruvate MR experiments, I compared build-up times and maximum signal generation using AH111501 and Finland radicals, and demonstrated that the AH111501 radical was superior to the Finland radical in both build-up time and maximum signal generated.

Finally, to optimise an anaesthetic protocol for future neuroimaging studies, I compared healthy rats at 100%, 90% and 60% inspired oxygen, and demonstrated reduced cerebral perfusion and dysregulated cerebral metabolism with hyperoxia.

Chapter 1 – Introductory Information

Multiple sclerosis (MS) is a chronic, demyelinating, immune-mediated disease which can affect any part of the central nervous system (CNS). Immune-mediated damage to the CNS causes both acute neurological dysfunction, and a more chronic, progressive neurodegeneration, which leads to accrued disability[1,2]. Lymphocyte infiltration drives acute demyelination and sclerotic plaque formation, while axonal damage and neuronal death result in widespread neurodegeneration[1,3]. At present, the pathophysiology of MS is incompletely understood, and though therapies have been developed which reduce the rate and severity of acute relapses, only one therapy is licensed for the progressive phase[4], and there is currently no cure. To rapidly develop new therapies and improve treatment selection and monitoring, effective imaging strategies are needed which are responsive to changes in disease activity[5]. Here, I sought to understand the role of hyperpolarised [1-^{13}C]ethylpyruvate MRS in the detection of inflammatory MS-like lesions in the delayed-type hypersensitivity/focal autoimmune encephalomyelitis rat model of MS.

1.1 Introduction to Magnetic Resonance Imaging and Spectroscopy

1.1.1 Proton Magnetic Resonance Imaging

Proton MRI is key to the current diagnostic and monitoring framework for MS. It utilises protons, primarily in water and fat molecules throughout the body, to provide *in vivo* structural (e.g. T_1 and T_2-weighted imaging), biophysical (MT and DWI images), or biochemical (proton MRS) information.

Protons possess the property of spin, which in the classical formalism of nuclear magnetic resonance (NMR), causes them to act like miniscule bar magnets in an externally applied magnetic field. When

such a field (B_0) is applied, protons may align with (parallel to) or against (antiparallel to) the field direction, thus producing two populations of oppositely aligned spins. In the quantum mechanical model, this is described in terms of low and high energy states, with a slight imbalance in the population sizes, and around 1ppm/T more protons populating the lower energy state than the higher energy state. Here, I will use the terminology of the classical model to describe magnetic resonance. The asymmetry between the number of parallel and antiparallel aligned protons is termed the polarisation of the sample, which produces a net longitudinal magnetisation in the direction of B_0.

Beyond simply aligning parallel or antiparallel to B_0, spins precess around the B_0 axis at a frequency determined by the strength of B_0 and the 'gyromagnetic ratio' (γ) of the spin – a constant unique to each different nucleus which determines how their resonant frequency changes with respect to the main magnetic field strength. This frequency is the Larmor frequency (ω) of the spins (Eqn 1).

(1) $$\omega = \gamma B_0$$

Irradiating protons in the B_0 field at their resonant or 'Larmor' frequency (usually in the radiofrequency (RF) range of the electromagnetic spectrum) induces a bulk transition of spins from the parallel to the antiparallel state, decreasing longitudinal magnetisation, as well as bringing the precession of the affected spins into phase with each other. After an RF pulse is delivered, the longitudinal magnetisation begins to relax, and the precessing protons begin to dephase. This dephasing is the result of both inhomogeneities in the B_0 field, producing local changes in resonant frequency, and due to the interactions between proton-containing molecules themselves, which each have a small local magnetic field which perturbs that around other protons, causing constant slight variations in resonant frequency as molecules move towards and away from each other.

The precession of spins in phase produces a net varying magnetic field, which can induce a voltage in a nearby 'receiver' coil, and it is this induced voltage which is recorded to provide information

about the properties of the protons being studied. The raw changing voltage detected is called a 'free induction decay' (FID). By altering the RF pulse bandwidth and duration, the number and timing of RF pulses, and the timing at which the FID is sampled and recorded, variables including the T_1, T_2 and T_2^* relaxation values of the protons in the tissue being sampled can be calculated: T_1 is a time constant related to the time taken for the longitudinal magnetisation to recover after an RF pulse, and varies according to B_0 and the temperature of the sample, while T_2 and T_2^* relaxation are related to rate of dephasing due to interactions between spins, and additional inhomogeneities in B_0 respectively.

To generate an image, there must be a method by which to recover spatial information from the FIDs picked up by the receiver coil. This is typically achieved using gradient coils, which provide time-varying magnetic field gradients in a given direction, and thus induce the Larmor frequency of nuclei in the sample to vary along the axis of the gradient. During an RF pulse, an initial 'slice select' gradient is delivered. The slice select gradient ensures that at the time the RF pulse is played, only a small proportion of the protons in the sample resonate within the frequency range of the RF pulse. Essentially, this selects out a slice of the sample which is perpendicular to the slice selection gradient. The thickness of the slice is dependent on the strength of the gradient and the bandwidth of the RF pulse. When the RF pulse ends, a 'phase encoding' gradient is applied in a direction perpendicular to the slice select gradient and causes the phase of the spins in the excited slice to vary along the direction of the phase encoding gradient. Finally, during the readout period, a 'frequency encoding' or 'readout' gradient is applied in a direction perpendicular to both the slice select and phase encoding gradients. The FID is sampled at multiple time points while the frequency encoding gradient is applied, and the induced voltage in the coil recorded.

Rather than sampling real space directly, in MRI, k-space – the frequency representation of real space – is sampled instead. The point sampled in k-space at each time point during the readout gradient depends on the 'area' under the phase and frequency encoding gradients: a product of the strength of the gradients, and the duration for which they are applied. k-space may be sampled by

varying the duration for which frequency and phase encoding gradients are applied. Typically, by varying the frequency encoding gradient while sampling at multiple time points, several points in k-space can be sampled per RF pulse applied. Performing a Fourier transform of k-space produces a series of waveforms which vary in their frequency, amplitude, wavelength, and direction. When summed over the whole image area, these waveforms interfere to produce an image[6–8].

1.1.2 Proton Spectroscopy

In contrast to imaging, in slice-selective spectroscopy the frequency of precession is used to encode chemical rather than anatomical information. Spatial localisation can be achieved using a 'surface coil' whereby the RF receiver coil which detects the FID is applied in close proximity to the sample or tissue of interest. Signal from the sample immediately adjacent to the receiver coil is detected, while that from tissue further away is not. Just as with imaging explained above, MR signal is obtained by induction of bulk transitions between nuclei parallel and antiparallel to B_0, however the frequency at which nuclei within a sample or a given compound precess is dictated not only by B_0, but by the chemical environment in which nuclei are positioned. Electrons produce a small magnetic field which 'shields' the nucleus from B_0, thus changing the effective field strength (B_{eff}) felt by the nucleus. This shielding effect is different depending on the position of a nucleus within a molecule. For example, acetic acid (CH_3COOH, Fig. 1a) contains four protons in two different environments: three protons surround one carbon atom and are adjacent to the carboxylic acid group. These protons have identical electron shields and will therefore experience the same B_{eff}. The fourth proton, however, is bonded to oxygen as part of the hydroxyl component of the carboxylic acid group, and as such its electron shielding is different to the other three protons in the molecule. It will experience a slightly different B_{eff} and resonate at a slightly different frequency to the other three protons in the molecule. This frequency difference is termed chemical shift (δ) and is defined in parts per million (ppm) relative to an arbitrary reference signal.

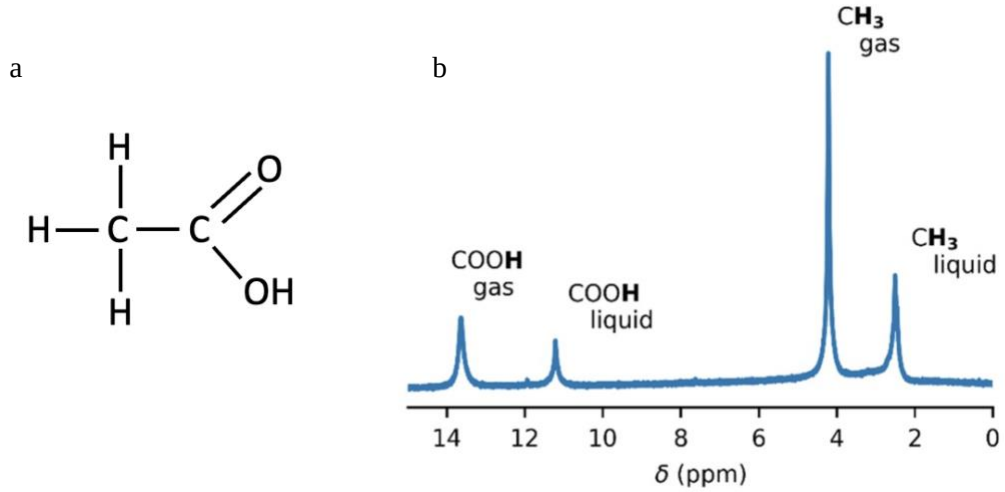


Figure 1. a) Chemical structure of acetic acid, CH_3COOH b) Example NMR spectrum of acetic acid (CH_3COOH) in the solid and liquid phases. Reproduced from Socha and Dračínský, 2020[9]

When a sample is excited by an RF pulse of appropriate bandwidth covering the resonant frequencies of both groups of spins, an FID is produced which is a composite of the individual signals from each distinct proton environment. Using a Fourier transform, this can be converted into a spectrum, with signal intensity on the y axis, and chemical shift on the x axis (see example in Fig. 1b). The area beneath each spectral peak relative to others in the spectrum gives information about the number of protons in each chemical environment. In our above example using CH_3COOH, the area beneath the CH_3 peak will be three times that beneath the COOH peak (Fig. 1b). The shape of each peak can be affected by a number of factors, including the mobility of the molecules represented by each peak, and the homogeneity of B_0[8].

1.1.3 Dynamic Nuclear Polarisation

Proton MRI has been the norm in clinical settings, as the abundance of protons in water and fat in living tissue make for high signal to noise ratio. This makes high spatial resolution and anatomical detail achievable even with relatively low percentage polarisation at biological temperatures and field strengths. However, several other biologically-relevant nuclei are amenable to MR imaging and spectroscopy[10]. For example, sodium imaging has been employed largely in neuroimaging to

create spatial maps of intracellular and extracellular sodium concentrations in the healthy and diseased brain[11], while phosphorus MR has been of use in studying tissue energetics and oncological metabolism[12]. Of importance in this project is that it is also possible to generate MR signal from the ^{13}C nucleus.

^{12}C is by far the most common carbon isotope in living systems. Only 1% of naturally occurring carbon nuclei are ^{13}C, and carbon is far less abundant in living systems than the hydrogen nuclei used in conventional proton MR. Typical polarisation levels at biologically viable temperatures and field strengths are in the order of 0.0005%[13], which results in very low signal to noise ratio (SNR) when applied to a nucleus as scarce as ^{13}C. However, using the process of dynamic nuclear polarisation (DNP), it is possible to generate extremely high polarisation levels (>50%), which provides sufficient signal for imaging and spectroscopy[13,14].

DNP relies on the polarisation of unpaired electrons in a donor free radical which is mixed in solution with the biological tracer of interest. At very low temperatures (~1K) and in a strong magnetic field (commonly between 3-7T), almost 100% polarisation is achieved among the population of unpaired electrons. Microwave irradiation is used to transfer polarisation from the unpaired electrons to the ^{13}C nuclei in the tracer. The addition of small concentrations of gadolinium can also be used to increase the level of polarisation generation by decreasing the electron T_1 of the radical[15]. The DNP process can increase the polarisation generated approximately 10,000-fold relative to conventional MR. Dissolution with a heated buffer solution brings the sample rapidly to biological temperature with the sample polarisation maintained, allowing rapid intravenous injection, and subsequent *in-vivo* imaging or spectroscopy[16].

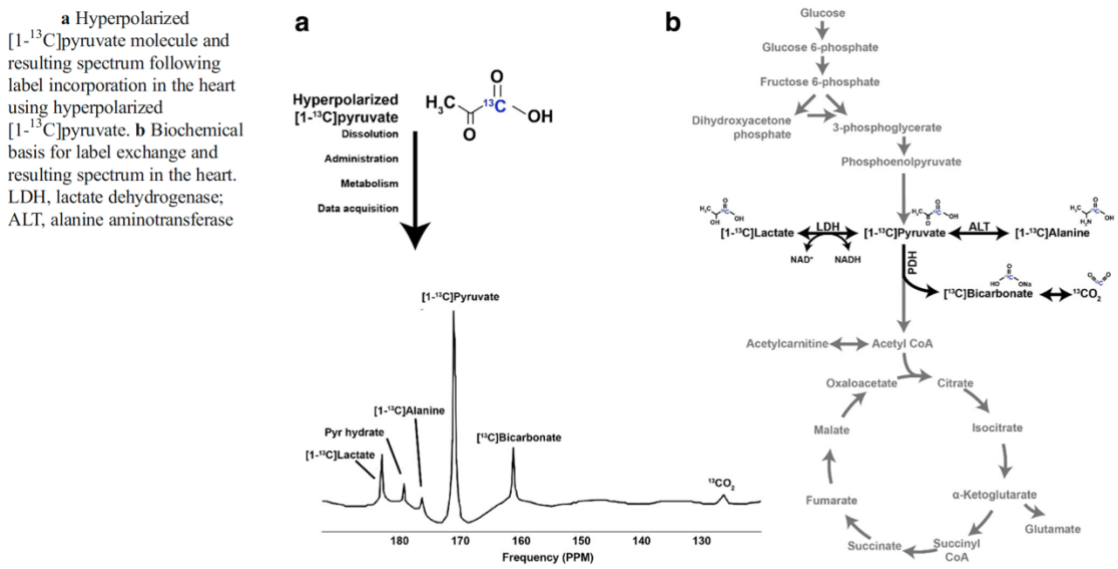
1.1.4 Hyperpolarised ^{13}C Magnetic Resonance Spectroscopy

The principles of proton MRS described above apply equally to hyperpolarised ^{13}C nuclei, the key difference being that polarisation is generated during the DNP process and decays exponentially

throughout the data sampling period, according to both the sample T_1, and the number and flip angle of RF pulses applied to it. At the point of dissolution, the sample polarisation begins to decay at a rate determined by the T_1 relaxation constant of the tracer molecule (approximately 50s *ex vivo* for [1-^{13}C]pyruvate, a commonly-used tracer[13]). This gives a relatively short window in which to gather data before the polarisation decays to an undetectable level – usually in the order of 1-2 minutes.

1.1.5 Pyruvate and Ethylpyruvate in Metabolism

To date, hyperpolarised ^{13}C MR has predominantly been used to probe cardiovascular and tumour metabolism[14,17]. Though many probes have been evaluated, the most commonly used is ^{13}C pyruvate. Pyruvate has favourable T_1 relaxation properties, allowing a relatively long window for data collection after injection, but perhaps more crucially sits at a key metabolic decision point.



a Hyperpolarized [1-^{13}C]pyruvate molecule and resulting spectrum following label incorporation in the heart using hyperpolarized [1-^{13}C]pyruvate. **b** Biochemical basis for label exchange and resulting spectrum in the heart. LDH, lactate dehydrogenase; ALT, alanine aminotransferase

Figure 2. From Lewis *et al*. 2020 Clinical Cardiovascular Applications of Hyperpolarised Magnetic Resonance[14]

Fig. 2, reproduced from Lewis *et al.*[14], demonstrates this. Pyruvate is generated as the end-product of the cytosolic glycolytic metabolism of glucose. Alternatively, after intravenous injection, pyruvate can be rapidly transported into cells via monocarboxylate transporters (MCTs)[18]. Pyruvate sits immediately before the committed step of several essential metabolic pathways and may have

several fates. These provide information about the overall metabolic state of the cell. The first fate is to enter the tricarboxylic acid cycle. Conversion of pyruvate to acetyl-CoA by pyruvate dehydrogenase (PDH) provides substrate for the tricarboxylic acid (TCA) cycle, used as the primary source of reduced cofactors for oxidative phosphorylation via the electron transport chain on the inner mitochondrial membrane. Conversion of pyruvate to acetyl-CoA generates carbon dioxide, which is in equilibrium with bicarbonate, hence rapid bicarbonate production indicates rapid TCA cycle turnover and extensive aerobic respiration via oxidative phosphorylation. Under anaerobic conditions, there is insufficient oxygen available to meet ATP demands through oxidative phosphorylation. Under these circumstances, glycolytic conversion of glucose to pyruvate provides rapid, but inefficient, ATP generation, with pyruvate being converted to lactate via lactate dehydrogenase (LDH), rather than entering the TCA cycle. Lastly, pyruvate may contribute to amino acid biosynthesis through conversion to alanine via alanine aminotransferase (ALT). Therefore, the balance of lactate and bicarbonate production (flux through LDH and PDH) can be used as a measure of the metabolic status of the cell[14].

These metabolic shifts can be detected with hyperpolarised ^{13}C MRS. Fig. 2 displays an example spectrum from a cardiac experiment using [1-^{13}C]pyruvate. The carbon at position 1 in the 3-carbon pyruvate molecule is cleaved during the production of acetyl-CoA and appears as bicarbonate signal, however lactate and alanine retain all three carbon nuclei from pyruvate after flux through LDH and ALT. The ^{13}C nuclei in each of the products have different chemical shifts, and hence have distinct spectroscopic peaks. By recording serial spectra after injection of the hyperpolarised tracer, the formation of metabolites including lactate and bicarbonate can be quantified, and hence the metabolic status of the sample tissue assessed dynamically *in vivo*[14].

A switch away from oxidative phosphorylation towards anaerobic lactate production is seen physiologically under conditions of aerobic strain such as exercise, however it can also be a marker of pathology. In cancerous cells, the well-documented ‘Warburg effect’ sees tumour cells switch towards anaerobic lactate production for energy production[19]. There is good evidence that a similar

shift is observable in inflammatory processes such as that in acute multiple sclerosis lesions. It is this switch I will investigate using hyperpolarised ^{13}C MRS in fEAE rat model of MS.

1.1.6 [1-^{13}C]Ethylpyruvate vs. [1-^{13}C]Pyruvate as a Hyperpolarised ^{13}C MRS Tracer Molecule for Neuroimaging

To provide useful metabolic information about the cells of the brain, a neurotracer must be able to cross the BBB. Unlike other organs, the brain is separated from the intravascular space by several specialised structures shown in Fig. 3, which form the BBB and tightly regulate the transcellular and paracellular transport of molecules from the blood into the brain[20]. As such, while tissues such as myocardium and tumour cells may readily uptake pyruvate from the extracellular space via MCTs, the delivery of pyruvate to the brain as a whole is limited to that which is transported across the BBB by MCTs[18].

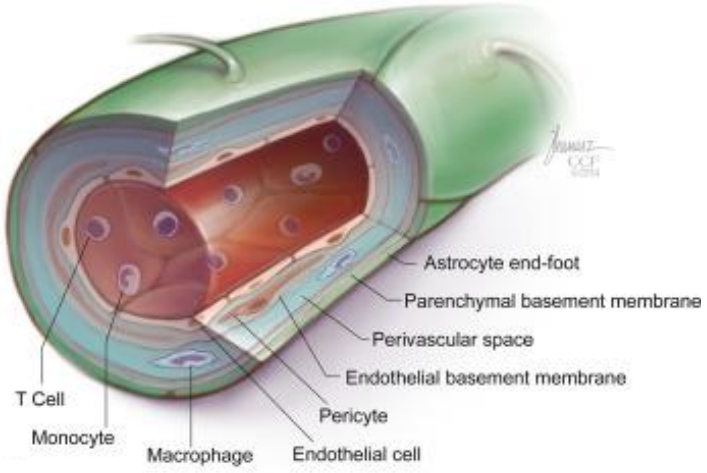


Figure 3. Cross-sectional diagram of the blood-brain barrier, reproduced from Obermeier *et al.*[20]

Miller *et al.*[21] demonstrated using hyperpolarised [1-^{13}C]pyruvate MRI in a rodent model of brain metastasis that lactate signal was only detectable at sites permeabilised by local BBB damage. Likewise, in the anaesthetised porcine brain, lactate signal was non-resolvable with an intact BBB,

however once the BBB had been permeabilised with mannitol, there was a 90-fold increase in pyruvate transport, and lactate production was visible throughout the brain.

However, [1-^{13}C]ethylpyruvate is a viable alternative to [1-^{13}C]pyruvate for hyperpolarised ^{13}C neuroimaging. Ethylpyruvate is an analogue of pyruvate, which is safe in humans and has been trialled as a possible anti-inflammatory therapy in its own right[22]. Ethylpyruvate is more lipophilic than pyruvate, which enables ethylpyruvate to circumvent the MCT transport system at the BBB by diffusing directly into the CNS, and is converted to pyruvate through non-specific esterases, allowing the same metabolic data to be gathered as if pyruvate itself had been injected[22,23]. In experiments in healthy rodents, Hurd *et al*. demonstrated that signal from injected hyperpolarised [1-^{13}C]pyruvate is restricted predominantly to the vasculature, with little contribution from the brain itself. Conversely, when repeated with hyperpolarised [1-^{13}C]ethylpyruvate, signal was significantly higher in the brain parenchyma than in the vasculature[24]. This was corroborated by Miller *et al.*, by demonstrating widespread endogenous pyruvate production in their rodent model of metastasis after hyperpolarised [1-^{13}C]ethylpyruvate injection[21]. These data suggest that due to its lipophilicity, and therefore rapid transport across the BBB, [1-^{13}C]ethylpyruvate represents an improvement over [1-^{13}C]pyruvate as a tracer for pre-clinical hyperpolarised ^{13}C neuroimaging.

1.2 Multiple Sclerosis

MS is the most common cause of atraumatic neurological disability in young adults. With a typical age of onset between 20 and 50 years, MS affects 2.3 million people worldwide and represents a significant resource burden on any healthcare system[5,25,26].

MS can affect any part of the CNS, producing a wide variety of neurological symptoms, including visual changes, sensory disturbances, motor symptoms, and autonomic dysfunction[1,2,5,27]. Typically, MS presents first with a clinically isolated syndrome (CIS)[1,5], defined as:

"patient-reported symptoms or objectively observed signs typical of an acute inflammatory demyelinating event in the CNS, current or historical, with duration of at least 24 hours, in the absence of fever or infection"[28]

This definition equally applies to the terms 'relapse' and 'attack' when applied to subsequent episodes of neurological dysfunction. Following a CIS, approximately 50% of patients will go on to experience further episodes of immune-driven neurological dysfunction[1], and it is usually at this stage that a diagnosis of MS can be made. Factors predictive of progression to a diagnosis of MS include young age at presentation, lesions in the spinal cord or infratentorial region, higher overall lesion load, presence of lesions which enhance with gadolinium (Gd)-based contrast agents using MRI, the presence of oligoclonal bands on cerebrospinal fluid (CSF) electrophoresis, and reduced velocity in visual evoked potentials[5]. A diagnosis of MS requires demonstration of primary CNS lesions disseminated in space (DIS) and disseminated in time (DIT). The precise diagnostic criteria for MS will be discussed in more detail below.

The natural history described above is that of the most common subtype of multiple sclerosis: relapsing-remitting MS (RRMS). In RRMS, patients experience discrete episodes of neurological dysfunction (relapses) which are punctuated by an almost complete recovery between episodes. Approximately 80% of MS patients will present with a relapsing-remitting disease course[1,5,28]. With time, approximately 65% of patients with RRMS progress to a disease stage in which they no longer make a full recovery between relapses. They begin to accrue disability progressively and recover incompletely from each relapse. This is classified as secondary progressive MS (SPMS), and while relatively good therapies currently exist to control relapses, only one treatment is licensed for the progressive stage of the disease. A small proportion of patients begin to accrue progressive disability from disease onset, and this subtype is termed primary progressive MS (PPMS)[1,5,28]. These subtypes are illustrated in Fig. 4. PPMS patients have more limited treatment options[4] and have a poorer prognosis than those with RRMS. More recently, there has been a shift to further characterisation of patients' disease course as 'active' or 'inactive' relapsing or progressive disease[29]. These terms are bound up with the concept of 'no evidence of disease activity' (NEDA) and are touched on in more depth below in section 1.5.

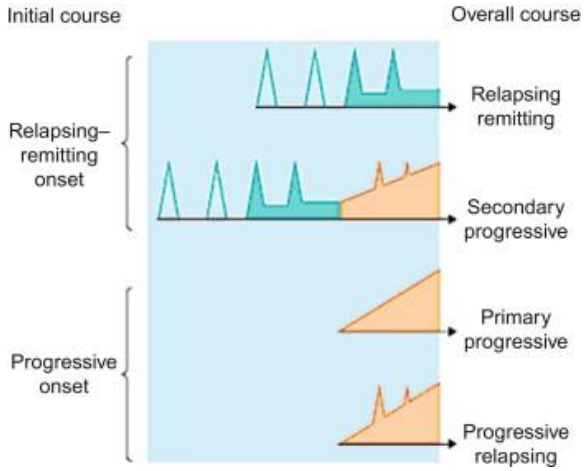


Figure 4. Varying disease course in multiple sclerosis subtypes, with neurological dysfunction on the y-axis plotted against time on the x-axis. Reproduced from Confavreux and Vukusic, 2014[30]

1.3 Pathogenesis and Pathophysiology of Multiple Sclerosis

1.3.1 Predisposition and Susceptibility to Multiple Sclerosis

Though much progress has been made in recent decades[3], the underlying pathophysiology of multiple sclerosis remains incompletely understood. That MS is an immune-mediated disease has been known for many decades due to the presence of abundant activated immune cells in histological examinations of MS lesions[3,31]. Genome-wide association studies have corroborated this link, by identifying multiple immune-related genes which affect the risk of developing MS, most prominently several included in the major histocompatibility complex (MHC) on chromosome 6[2,32]. Several lines of evidence implicate a specific adaptive immune response to certain CNS antigens, including the confinement of the inflammatory response to the CNS, the presence of B and T cell populations derived from clonal expansion, and the presence of discrete oligoclonal bands in CSF analysis of patients with MS[31]. Despite no individual CNS antigen having been definitively pinpointed as being the immune target in MS, reactions against several self-antigens, such as myelin basic protein (MBP) and myelin oligodendrocyte glycoprotein (MOG) have been implicated[33]. Injection of MBP/MOG or MBP/MOG-reactive T cells can generate an MS-like autoimmune

encephalitis in several animal species[31,34], while MBP-reactive T cells have been found to undergo clonal expansion and accumulation in the CNS in MS patients[33].

Nevertheless, several theories give a plausible explanation as to what may initiate an immune reaction in the first place. Firstly, several factors have been identified which increase an individual's risk of developing MS. Genetics certainly play a role, with parents and siblings of MS patients much more likely than population probability to develop the disease themselves[1]. Further, over 200 genes have been implicated in altering MS risk, and 31 of those are linked to MHC genes involved in antigen presentation and lymphocyte activation[2,35], cementing the link with immunity.

Environment plays a role in MS risk as well. Geographically, there is a trend for higher rates of MS in populations further from the equator, and of Northern European descent[25]. However, individual risk seems to be more connected to the location in which a patient spends their childhood than to the ethnic group or geographical location of their birth. Linked to this geographical distribution of MS prevalence, those with low vitamin D levels are more likely to develop MS, as are those who smoke cigarettes, and those who have encountered infectious agents such as Epstein-Barr virus (EBV). The overall rate of MS worldwide has been steadily increasing, and aside from greater efficiency in diagnosis, one possible explanation is the 'hygiene hypothesis': the generation of aberrant immune responses in later life to pathogens ordinarily encountered early[1,2,31,36], which has emerged with an overall global improvement in living standards in recent decades.

1.3.2 Pathogenesis of Multiple Sclerosis

In susceptible individuals, there must still be a priming action which begins the immune response. With CNS antigens sequestered behind a BBB theoretically impermeable to peripheral immune cells, there is much debate as to whether this first event happens within the CNS behind the BBB, or in the periphery. The 'inside out' theory relies on the idea that an initial inflammatory event takes place within the CNS, producing tissue damage and BBB breakdown, and release of CNS antigens

into the periphery. Here, autoantigens are presented to peripheral immune cells that migrate to the CNS and begin an immune attack. This theory has been advanced most strongly by Stys *et al.*[37] who contend that MS should in fact be classified as a primary neurodegenerative disease. They cite, among other evidence, that myelin damage may precede inflammatory cell infiltration, and the ineffectiveness of anti-inflammatory therapies in treating the progressive phase of MS to conclude that inflammation in MS is in fact a reaction to exposed myelin breakdown products secondary to primary destruction of oligodendrocytes – the glial cells responsible for myelin sheath production in the CNS.

The 'outside-in' theory, asserts that an event outside the CNS produces an immune response directed against CNS antigens[32]. There is an element of immune surveillance within the CNS by peripheral lymphocytes under normal circumstances, with small numbers of immune cells trafficking in and out of the CNS in search of pathogens, particularly at the choroid plexus[38]. Trafficking of autoimmune lymphocytes into the CNS which encounter self-antigens such as MBP may be enough to begin an immune response. Alternatively, the priming event may be something as trivial as trauma which disrupts the BBB, or an infection which temporarily increases BBB permeability through direct damage or by cytokine release. It has been observed that BBB breakdown can be detected before immune cell infiltration in early MS lesions[36,39], and further that early MS lesions show deposition of fibrinogen, an indicator of endothelial permeability. Fibrinogen has been shown to activate microglia in the absence of an adaptive immune response[40], and it is conceivable that a 'perfect storm' of genetic and environmental factors conspire to generate an initial BBB permeability which allows pro-inflammatory fibrinogen deposition in the CNS thereby providing a route for peripheral immune cell migration into the CNS, and ensuring that on arrival they contact CNS antigens in a pro-inflammatory environment generated by fibrinogen-activated microglia conducive to immune activation[36].

In either case, there must be an adaptive immune component which is ready to react to autoantigens. During immune maturation, autoreactive T cells (T cells with T cell receptors (TCRs) against

epitopes of 'self' antigens) should be selected out, however this process is not completely effective, and some autoreactive T cells inevitably remain[31]. These may never encounter their autoantigen, but if they do, they will have the capacity to generate a specific autoimmune response. In addition, TCRs can bind several epitopes of similar molecular structure. This becomes a problem when pathogenic epitopes physically resemble elements of 'self' molecules – a phenomenon called molecular mimicry. Several EBV epitopes are almost identical to those of MBP, and it is possible that molecular mimicry between these and other pathogenic epitopes may be responsible for the initial immune priming in MS[1,2,31]. Lastly, an overwhelming, systemic, pro-inflammatory immune response to any cause can produce 'bystander activation' of lymphocytes, whereby they become activated without contact with any specific antigen[31]. These activated lymphocytes are then free to enter the CNS if BBB permeability allows and generate a local pro-inflammatory immune response. However lymphocytes are activated initially, their abundance in acute MS lesions[3], the presence of B cell-rich lymphocytic deposits in the meninges[31], and the efficacy of lymphocyte-modulating therapies in MS treatment[4,41–43] makes it clear that an adaptive immune response against myelin-related or oligodendrocyte proteins is key in the generation of acute MS lesions.

Once an immune-mediated reaction is established, the classic pathological finding in MS is the demyelinated, sclerotic plaque. Lymphocytic infiltration dominated by T cells, particularly those reactive to MBP epitopes, but also containing B cells and plasma cells, produces a pro-inflammatory environment further perpetuated by the activation of local microglia, and chemotaxis of peripheral macrophages[33]. In an acute lesion, cytotoxic cluster of differentiation (CD) 8^+ T cells induce apoptosis in oligodendrocytes. $CD4^+$ T helper populations including Th_1 and Th_{17} cells[44] produce pro-inflammatory cytokines, which activate microglia and macrophages. Th_{17} cells in particular release interleukin (IL) 17 and IL22, which act to increase BBB permeability, allowing further peripheral immune cell migration into the CNS[1,45]. This typically forms a ring of activated T cells and microglia, which surround a core of activated macrophages and lymphocytes[1,3].

Within the acutely inflamed lesion, several processes take place in addition to the direct action of cytotoxic and phagocytic activated immune cells which result in oligodendrocyte death and axonal damage. Activated macrophages and microglia produce matrix metalloproteinases (MMPs), which are partially responsible for the degradation of myelin proteins and may also play a role in allowing immune cell migration across the BBB into the CNS[36]. In an experimental autoimmune encephalitis model, knock-out of MMP-2 and MMP-9 prevented T cell infiltration beyond the basement membrane of the BBB, conferring protection against generation of encephalomyelitis[46]. Further, activated microglia produce reactive oxygen species (ROS) and reactive nitrogen species (RNS) which produce oxidative damage to neuronal and oligodendrocytic proteins, and specifically to neuronal mitochondrial proteins[32,47–49]. Macrophages exhibit increased nicotinamide adenine dinucleotide phosphate (NADPH) oxidase activity, which marks oxidative damage to CNS tissues[3], and the inflammatory milieu in the lesion core contains cytotoxic factors such as perforin[37] which independently damage CNS cells.

Even once the initial acute inflammatory reaction has died down, inactive lesions continue to display an element of microglial activation, and in fact activated microglia can be found throughout the 'normal-appearing white matter' (NAWM) in the progressive phase of the disease[3,32]. A degree of remyelination is possible thanks to reservoirs of mature precursor oligodendrocyte cells, which allow a proportion of damaged axons to be recovered, and inflammatory debris is removed by M2 macrophages[3,31,50]. However, this capacity for remyelination is finite, as the oligodendrocyte precursor populations gradually deplete[1]. Neuronal survival, even for cells which have undergone demyelination, is common beyond the cessation of acute focal inflammation, however neurons which are not remyelinated lack the trophic support usually provided by oligodendroglia, and eventually cell death occurs[2,51].

Cumulative cell death throughout the MS brain is thought to account for the gradual symptom accumulation seen in the progressive phase of the disease, and there is much debate regarding the exact mechanism by which this degeneration occurs[1,37,51]. It is likely that diffuse axonal damage and

cell death is a result of interplay between multiple concurrent pathological mechanisms, several of which are outlined below.

There are similarities between the pattern of cell death in MS and in ischaemic stroke[52], which have led to the concept of 'virtual hypoxia', which refers to a series of maladaptive processes which converge on an inability to maintain adequate oxidative ATP generation in affected neurons, leading to cell death in a similar manner to that observed in true hypoxia. Chronic microglial activation downregulates peroxisome proliferator-activate receptor gamma coactivator 1α (PGC1α), reducing transcription of antioxidants and respiratory chain subunits[32], while ROS and RNS have been shown to damage mitochondrial DNA (mtDNA). This inhibits transcription of respiratory chain subunits, and further, direct damage to respiratory chain proteins by ROS and RNS, impairs the function of those that remain[49]. Reduced mitochondrial oxidative adenosine triphosphate (ATP) generation induces an energy deficit within neurons that results in further ROS production, perpetuated by reduced antioxidant generation, resulting in more oxidative damage.

With loss of the oligodendrocyte myelin sheath, conduction velocity is impaired by the loss of efficient saltatory conduction. In response, there is a reorganisation of voltage-gated sodium channel distribution, whereby sodium channels are increased in number and positioned more evenly along the length of the axon, no longer clustering at Nodes of Ranvier. This reorganisation is not inherently pathological, and resembles that seen in non-myelinated axons, however it increases sodium leak across the axolemma. Consequently, the sodium-potassium ATPase must increase its rate of activity to maintain the sodium gradient across the axon membrane, raising the ATP demand of the cell[49,53,54]. In naturally unmyelinated axons, mitochondrial number is increased, however with the concurrent impairment in mitochondrial function described above, demyelinated axons are unable to increase their rate of oxidative phosphorylation to meet this increased demand. With rising intracellular sodium concentration and insufficient ATP generation to restore baseline transmembrane sodium gradients and resting membrane potential, neurons become hyperexcitable, undergoing numerous unnecessary, inefficient depolarisations, which further increase the workload

of the Na^+/K^+ATPase pump[51]. Ultimately, rising intracellular sodium levels reverse the axolemmal sodium-calcium exchanger, precipitating a rise in intra-axonal calcium concentration[53]. Perpetuating this rise in intracellular calcium concentration is the phenomenon of glutamate excitotoxicity[51]. Glutamate levels are increased in the extracellular milieu surrounding demyelinated neurons by release from immune cells, vesicular release from neurons themselves[2], and reversal of the axonal sodium-dependent glutamate transporter. Ionotropic glutamate receptors are permeable to calcium ions and have been found to be functionally coupled to intracellular calcium stores. Their overactivation by accumulated extracellular glutamate, in addition to calcium influx through the reversed Na/Ca exchanger precipitates a lethal increase in intracellular calcium, which induces cell death[51].

Lastly, in recent years there has been a shift in thinking from considering MS to be a primarily immune-mediated disease comprised of multiple acute flares, with neurological symptoms related to lesion size and position, to a recognition that a significant component of disability is caused by a neurodegenerative process, which results in continued axonal loss throughout the normal-appearing white and grey matter (NAWM and NAGM) outside of acute lesions and between relapses. This more diffuse NAWM and NAGM pathology is thought to be responsible for accrued disability in PPMS and SPMS. Some authors have gone as far as to suggest that MS is primarily a neurodegenerative disease, with non-inflammatory neurodegeneration precipitating a secondary immune reaction[37]. Other groups have noted that there is widespread microglial activation outside of acute lesions, and that this may be responsible for the diffuse axonal damage seen in the progressive phase of the disease. Cortical grey matter damage may reach 75% in some patients, and is topographically linked to meningeal lymphocytic deposits, similar to tertiary lymphoid tissue, that are rich in $CD4^+$ T cells, B cells and plasma cells[32]. It has been suggested that the secretion of a diffusible factor precipitates axonal damage in the underlying cortex[31].

1.4 Diagnosis of Multiple Sclerosis

Diagnosis in MS relies primarily on the demonstration of two or more primary demyelinating CNS lesions occurring at different times, and in distinct areas of the CNS: DIT and DIS[5]. The gold standard pathway for MS diagnosis is laid out in the McDonald Criteria[5]. These criteria aim to distinguish MS, with high specificity, from similar disorders such as neuromyelitis optica (NMO), NMO spectrum disorder (NMOSD), functional or somatisation disorders and other conditions which can mimic MS, whilst maintaining high sensitivity. In RRMS, history taking and clinical examination demonstrating evidence of attacks from two or more of four distinct anatomical areas of the CNS which are commonly affected in MS (periventricular, juxtacortical and infratentorial white matter, or spinal cord), and separated by time are sufficient for a diagnosis of MS. Where there is diagnostic uncertainty, or when only a single clinical presentation has occurred, paraclinical investigations are employed: MRI, CSF analysis by lumbar puncture, and visual evoked potentials, alongside serum biomarkers of NMO/NMOSDs: anti-aquaporin-4 (AQP4) and anti-MOG antibodies[5,28].

The McDonald criteria currently include recommendations for imaging criteria based on Gd-enhanced and T_2-weighted brain MRI[5]. Gd-enhancement is a marker of blood-brain barrier (BBB) breakdown, which is typically associated with acutely inflamed lesions as Gd-enhancement takes place only in the first three weeks or so after development of a new lesion[55]. T_2 lesions depict the 'footprint' left behind after previous inflammation[56]. As with clinical examination above, MRI evidence of two or more lesions in separate CNS areas is sufficient to demonstrate DIS. DIT can be demonstrated in two ways. Firstly, by visualising Gd-enhancing and non-Gd-enhancing lesions on a single scan. Gd-enhanced scans are currently the only validated imaging method by which to assess lesion chronicity, and the presence of both Gd-enhancing and non-Gd-enhancing lesions on a single scan indicates lesions with substantially different onset times. Secondly, the presence of new T_2 lesions on follow-up MRI scans when compared to a patient's baseline scan is also sufficient

to demonstrate DIT[5,28]. For patients with multiple recurrences of similar symptoms, suggesting repeated bouts of inflammation at a single site, diagnosis is more complicated. A more comprehensive description of the MS diagnostic framework can be found in reference 5[5]. In cases of diagnostic uncertainty, the presence of spinal MRI lesions in addition to brain lesions on MRI may be sufficient for a diagnosis of MS. Likewise, the presence of two or more oligoclonal bands on CSF electrophoresis that are not present on electrophoresis of paired plasma samples can stand as evidence of DIT. If there are clinical or radiological features of MS which do not fulfil the McDonald criteria, then re-scanning at 3-6 months is recommended, and again after 6-12 months if further evidence is needed[56].

In PPMS, the diagnostic criteria are different. These patients must display progressive loss of function for a period of at least one year from onset, in addition to displaying at least two of the three following features: at least one T_2 brain lesion situated at the anatomical sites listed above, multiple spinal cord lesions, or the presence of oligoclonal bands on CSF examination[5].

The most recent, 2017, update to the McDonald criteria relies on T_2-weighted MRI and post-Gd contrast-enhanced scanning for MS diagnosis, and the most recent MAGNIMS recommendations laid out a standardised protocol for investigation of possible MS patients[5,57]. Axial proton density T_2-weighted images and/or axial T_2-FLAIR images should be accompanied by sagittal T_2-FLAIR images. 3D FLAIR images are preferred, providing improved visualisation of the infratentorium compared to 2D-FLAIR, however the authors note that axial T_2-FLAIR provides improved visualisation of juxtacortical and periventricular lesions, but is inferior for detection of infratentorial lesions compared to T_2-weighted images[57]. T_2-weighted images remain the reference standard for lesion detection. Diffusion-weighted imaging (DWI) is currently included as an optional sequence, which can distinguish MS lesions with high diffusion coefficients, from ischaemic lesions with low diffusivity[5,57,58].

Advanced MRI techniques such as proton magnetic resonance spectroscopy (MRS) and magnetisation transfer (MT) imaging have shown use in the assessment of both acute lesions and diffuse grey and white matter disease. MRS offers a radiation-free, non-invasive method of estimating *in-vivo* concentrations of various metabolites. A myriad of molecules have been examined with MRS, but in the acute MS lesion, choline and lactate have been noted to increase. Lactate is a marker of acute inflammation, and the mechanisms by which it becomes elevated in the MS lesion are discussed in detail in section 4.1. In identifying this local increase in lactate in acute MS lesions, proton MRS has aided in providing a biochemical basis for the ^{13}C spectroscopy used in Chapter 4 of this project. A lesional increase in choline concentration denotes increased rates of phospholipid membrane breakdown, underscoring and biochemically corroborating the importance of demyelination in the acute lesion as part of MS pathophysiology[59]. Another key metabolite in proton MRS examination of MS is N-acetylaspartate (NAA). NAA is produced almost exclusively in neurons, and as such is used as a marker of neuronal metabolism and is decreased in MS lesions. Typically, the reduction in NAA concentration is reduced further from the core of an active lesion. However, NAA is also decreased throughout the NAWM and independent of acute lesions, which contributed to the re-examination of MS pathophysiology through the lens of neurodegeneration and axonal damage described above in section 1.3. Further, proton MRS adds weight to the role of glutamate excitotoxicity in neuronal damage, particularly in the progressive phase of the disease, identifying increased glutamate concentrations in the NAWM[59,60].

MT imaging, has also been highlighted as predictive of disability and cognitive decline[58]. Advanced MRI has demonstrated a trend towards a greater degree of generalised tissue damage in the NAWM in MS relative to several allied conditions including NMO, acute demyelinating encephalomyelitis (ADEM), and Leber's hereditary optic neuropathy (LHON), potentially providing an extra means by which to distinguish MS from these conditions in the future. However, these techniques require further development and validation before they are introduced into future recommendations[57,58]. In particular, proton MRS suffers from the lack of a 'smoking gun' metabolite alteration that can identify MS with high sensitivity and specificity. No individual metabolite has been demonstrated

to be consistently altered with sufficient effect size to be used alone in MS diagnosis. Further, a reduction in NAA – the most widely reproduced single-metabolite effect in MS – is non-specific, with similar changes seen in other conditions such as diabetes mellitus and systemic lupus erythematosus. In addition, lack of standardization in scanning protocols and parameters, data processing and spectral quantitation, and the consistent production of high-quality data has been a barrier to the clinical implementation of proton MRS. It seems most likely that future applications of proton MRS in MS diagnosis will involve complex consideration of multiple metabolite changes to identify a biochemical 'fingerprint' of MS, which enhances the technique's sensitivity and specificity[60].

Beyond diagnosis, imaging is an essential part of treatment monitoring and therapeutic development in MS. To an extent, imaging can predict conversion from CIS to MS, and give prognostic information about likely accrued disability[56,61]. Further, it is part of the work-up of patients at each new relapse. MAGNIMS recommends that all patients should undergo a repeat brain MRI after each attack. Ideally, repeat MRI scans should use the same clinical system and parameters as a patient's baseline imaging[56].

The advanced imaging techniques outlined above are set to enhance the sensitivity of treatment monitoring as well as diagnosis. MT imaging has already shown alemtuzumab to be protective against grey matter damage[62], highlighting the importance of these advanced techniques in the assessment of diffuse as well as focal disease. Further, a key goal in imaging development is to identify those 'non-responders' among newly treated patients who would be better treated by second- or third-line therapies. Currently, Gd-enhanced imaging can detect BBB breakdown, which is typically present for approximately 3 weeks after lesion formation. Following this, monitoring largely relies on monitoring of the size and number of T_2-weighted lesions[56]. Imaging techniques which can assess lesion chronicity beyond subdivision into pre- and post-week 3 of development, and which are able to track individual lesion activity rather than simply lesion size or number would be of great use.

The authors of both the 2010 and 2017 updates of the McDonald criteria comment that new imaging techniques and modalities are likely to be incorporated into imaging guidelines for MS in future revisions, and highlight research into MS imaging as a key area for the progression of MS diagnosis[56,57]. Techniques which can detect lesions in the pre-symptomatic phase, and which can assess lesion chronicity would be of particular use. Imaging techniques sensitive to the underlying metabolic activity of a lesion or set of lesions, rather than their physical structure may be of use in this regard. One such approach, proton MRS, has already been briefly discussed above, and another, ^{13}C hyperpolarised MR spectroscopy and imaging, is the subject of this project and will be discussed here in detail.

1.5 Multiple Sclerosis Treatments

Underscoring the immune-mediated nature of MS pathogenesis, the management of MS relies almost exclusively on various forms of immune suppression. In an acute relapse, it is typical to dampen the acute inflammatory reaction using 3-5 days of high-dose corticosteroids, usually methylprednisolone[1,2,463].

The underlying disease process is controlled using 'disease modifying therapies' or DMTs. These are a group of therapies designed to target specific components of the immune machinery to reduce relapse rate and disability accumulation. There are a multitude of drugs licensed for the treatment of relapsing forms of MS. Several of the most important will be discussed here.

Natalizumab is a humanised monoclonal antibody which targets the $\alpha 4\beta 1$ integrin, inhibiting transendothelial trafficking of lymphocytes into the CNS, and is very effective in reducing relapse rate[43]. Fewer lymphocytes are able to access areas of focal neuroinflammation reducing the overall level of inflammation generated, and with it, demyelination, axonal damage, and symptoms. Fingolimod is another therapy which relies on preventing the arrival of lymphocytes at sites of

potential lesion formation. Fingolimod, and its analogues siponimod and ozanimod, are sphingosine-phosphate receptor (S1PR) inhibitors[4]. S1PRs have many functions, and may have a role in the regulation of BBB permeability[64], but their key function with respect to MS treatment is that they aid the egress of lymphocytes from secondary lymphoid tissue[65]. Their inhibition sequesters lymphocytes at lymph nodes and other secondary lymphoid sites, and prevents pro-inflammatory lymphocytes from reaching the CNS[4]. Preclinically, fingolimod has been demonstrated to limit demyelination and preserve neuronal function in multiple models of MS[66–68], while phase 2 and 3 clinical trials have shown it to be more effective than placebo in reducing relapse rate, lesion burden and disease progression, and to be superior to interferon beta-1a in reducing relapse rate and radiological measures of disease activity[42,69].

Almost all MS therapies, and those discussed above, are licensed only for use in relapsing forms of MS. There is currently only one licensed treatment for PPMS, and that is the humanised monoclonal antibody ocrelizumab[4]. Ocrelizumab targets the B-cell surface molecule CD20, which is present on all but the most immature and most mature B cell populations. Because of this, ocrelizumab can target the vast majority of B cells for destruction while leaving immature cells for immune reconstitution and retaining humoral immunity through mature plasma cells. Ocrelizumab has been shown to be highly effective in reducing relapse rate, but crucially also at reducing progression in PPMS patients[2,4,41].

Clinical strategies have evolved since the first DMTs were first introduced in the mid-1990s. Classically there have been two approaches to DMT selection widely employed. The ‘escalation’ strategy involves starting with a less effective, but well-tolerated DMT, and progressively introducing more potent DMTs if patients continue to exhibit poorly-controlled disease. This approach stems from the trend that the most effective DMTs tend to have the most severe side effects[2]. For example, an immunosuppression-related reactivation of the John Cunningham (JC) virus called progressive multifocal leukoencephalopathy is known to occur with multiple DMTs including fingolimod and particularly with natalizumab[70]. Other side effects common to multiple

DMTs include risks from opportunistic infections such as cryptococcus, varicella zoster, and herpes viruses[4]. More recently however, the preferred treatment strategy has been the 'induction' strategy. In this strategy, highly effective therapies are introduced as early as possible either in those with a new diagnosis of MS, or in those with a CIS and a high probability of progression to MS. The idea is to gain rapid control over relapses and new lesion formation, thereby hopefully reducing disease progression and disability accumulation[4]. The impact that DMTs have had on disease course is demonstrated in that time from diagnosis of RRMS to SPMS has increased markedly in the decades since the introduction if DMTs[2]. Further, with improved early diagnosis facilitating early treatment with DMTs, and general improvements in population health, the overall severity of disease presenting to outpatient MS clinics has declined. This has led to a recent reframing of treatment intent towards achieving NEDA: a triad of no relapses, no disability accumulation, and no new MRI changes. Those patients in whom NEDA has been induced may be said to exhibit 'inactive' relapsing or progressive disease. Those with ongoing symptoms or radiological change remain 'active'[29].

In addition to managing the underlying disease process, it is important to manage individual symptoms which arise from neurological dysfunction, for example pain, spasticity, bladder dysfunction, sexual dysfunction, and depression[1].

1.6 Animal Models of Multiple Sclerosis

To date no species have been identified that naturally develop MS except humans[71]. CNS biopsy does not form part of the diagnostic or monitoring framework for MS, and as such there is a paucity of human CNS tissue available to study the human disease, particularly during its early stages. Post-mortem is uncommon, and therefore even tissue from deceased patients is difficult to source. Therefore, as with many diseases, preclinical animal models of MS have been, and continue to be, instrumental in identifying elements of the pathophysiology of MS, and in developing new

therapies. Many approaches have been generated to approximate various elements of MS pathology, but none completely encapsulates all aspects of the disease. Several of the most common disease models are discussed briefly here, but they have been reviewed more extensively by other authors[34].

Before discussing individual animal models, it is important to note several factors that impair the direct translatability of mouse model data to human subjects which apply to all animal models of MS. First, the 'prime mover' in MS initiation is as yet unknown, and therefore all currently used methods of initiating an MS-like pathology in animals are artificial. Second, animal models tend to be designed to produce a rapid disease onset – typically days to weeks. While this facilitates rapid research turnover, it contrasts with the human disease, which can progress subclinically for months to years before becoming symptomatic. Thirdly, all of the most common MS models are rodent models generated in relatively in-bred, genetically homogeneous populations, which may be genetically predisposed to certain reactions in response to immune or toxic stimuli which may not be reproducible in other animals. Lastly, though there are many similarities between the human and rodent immune systems, they are not identical, and therefore any extrapolation from rodent to human pathophysiology should be treated with caution[34].

1.6.1 Experimental Autoimmune Encephalomyelitis

The most common animal model of MS is the experimental autoimmune encephalomyelitis (EAE) model[72]. This encompasses a group of related models in which an animal is immunised with self-CNS proteins or protein fragments, usually in the presence of an immunopotentiator such as Freund's adjuvant or pertussis toxin. Commonly used proteins include MBP, proteolipid protein (PLP), and MOG, and this model can be applied in multiple different animals, including monkeys[73] and guinea pigs[74], but is usually applied to rodents. Alternatively, encephalitogenic T cells from a donor animal may be transferred into a target animal, generating a similar immune response, or more recently, transgenic mice engineered not to undergo the usual T-cell receptor (TCR)

recombination process can be induced to express TCRs specific for certain self-CNS proteins or epitopes. In these transgenic models, EAE may be generated spontaneously, without peripheral immunisation with self-proteins[34,75].

Where MS is typified by a $CD8^+$-dominant lymphocytic infiltration in the core of an acute demyelinating lesion[3], $CD4^+$ T cells appear to be the dominant effector cells in EAE. Th_1 and Th_{17} cells are both found in EAE lesions, and have been noted in MS lesions as well[34]. Further, there is evidence that T_{reg} and B cells play a role in EAE pathogenesis[3,76], further mimicking the human disease. However, lesion generation in EAE models of MS tends to be typically restricted to the brain and spinal cord white matter, whereas significant grey matter and cortical disease is seen in MS, particularly in patients in the progressive phase of the disease. Depending on the rodent line used and the self-protein epitopes used for immunisation, EAE can mimic the acute or chronic MS lesion. However, it does not accurately model the progressive neurodegenerative phase of the disease[34].

1.6.2 Viral Multiple Sclerosis Models

A second method of inducing MS-like demyelinating lesions in rodent models is through induction of demyelinating viral infections. Theiler's murine encephalomyelitis virus (TMEV) relies on infection with a neurotropic picornavirus which induces neuronal damage and cell death. While TMEV is primarily a non-immune model, and requires persistent viral infection to induce pathology, neuronal cell death provokes an immune response which results in demyelination and oligodendrocyte death[77]. It is therefore most commonly used to study axonal damage and remyelination[34].

1.6.3 Toxic Multiple Sclerosis Models

Toxin-induced demyelination represents another method by which to study MS. Adding the copper-chelating agent cuprizone to mouse chow produces oligodendrocyte death and demyelination through oxidative stress on highly metabolically active oligodendrocytes by inhibition of copper-dependent cuproenzymes[78,79], and is useful in studying mechanisms of demyelination and remyelination, as cuprizone-fed mice exhibit remyelination with the cessation of the cuprizone diet. Several other toxins such as lysolecithin and ethidium bromide have been shown to produce demyelination by different mechanisms. Criticisms levelled at toxin-based MS models apply to all: the mechanism of initiation of demyelination is not related to that in MS, these are primarily non-immune-mediated models and as such can only comment so far on the pathophysiology in human disease, and that these models typically do not respond to immunomodulatory treatment, so are typically not used in treatment development[34].

1.6.4 Focal Experimental Autoimmune Encephalomyelitis

Lastly, it is possible to induce highly reproducible, anatomically specific MS-like lesions with the focal experimental autoimmune encephalomyelitis, or focal delayed-type hypersensitivity (DTH) model of MS[66,80]. Stereotactic injection of heat-treated Bacille Calmette-Guerin (BCG) into the CNS followed by peripheral sensitisation with BCG and an immunopotentiator can be used to produce a type IV hypersensitivity reaction at the site of injection. The lesion produced exhibits an inflammatory core of lymphocytes and activated macrophages, surrounded by a rim of activated microglia, similar to an acute RRMS lesion[80,81]. Limitations of this model include producing only one lesion and providing no information regarding the progressive phase of the disease. On the other hand, its value lies in the ability to predict precisely where and when a lesion will develop, and to employ the unaffected hemisphere as a paired control. Further, the DTH lesion is well-

characterised[82,83], and the response of the DTH model to treatment with fingolimod has been evaluated previously[66].

Summary of Chapters

In this thesis, I have investigated the use of hyperpolarised [1-^{13}C]ethylpyruvate magnetic resonance spectroscopy (MRS) in detecting acute inflammatory lesions in the brain of the focal experimental autoimmune encephalomyelitis rat model of multiple sclerosis, and sought to improve dynamic nuclear polarisation and anaesthetic protocols to optimise signal and cerebral perfusion under anaesthesia respectively. This work begins to provide a baseline from which to build translational work with hyperpolarised [1-^{13}C]ethylpyruvate imaging, which may result in an improved modality for MS disease monitoring, treatment selection and drug development in the future.

In chapter 2, I present data from dynamic nuclear polarisation experiments in which I tested a [1-^{13}C]ethylpyruvate mixture previously validated using the AH111501 trityl radical, against mixtures containing an alternative radical (Finland) with varying concentrations of gadolinium contrast agent.

Chapter 3 demonstrates the effects on cerebral perfusion of varying inspired oxygen concentration in rats under anaesthesia using perfusion magnetic resonance imaging (MRI) and hyperpolarised [1-^{13}C]pyruvate spectroscopy.

Chapter 4 examines the use of hyperpolarised [1-^{13}C]ethylpyruvate spectroscopy in the evaluation of brain lesions and their response to fingolimod treatment in the focal experimental autoimmune encephalomyelitis rat model of multiple sclerosis.

In chapter 5, I reflect on the skills and techniques I have gained during this degree, and on some of the challenges I have faced this year and what I have learned from them.

Chapter 2 – Optimising an [1-^{13}C]Ethylpyruvate Mixture for DNP

2.1 Introduction

As explained in chapter 1, the increased lipophilicity of ethylpyruvate relative to pyruvate makes it a promising candidate tracer for neuroimaging[24], allowing ethylpyruvate to access the CNS via simple diffusion to an extent which is not achievable with pyruvate in the presence of an intact BBB[21] . Within the CNS, [1-^{13}C]ethylpyruvate is hydrolysed to form [1-^{13}C]pyruvate, which enters cerebral metabolism, giving the same metabolic information as if [1-^{13}C]pyruvate itself had been injected[24].

Previous work in our group had ascertained the optimum composition a mixture of [1-^{13}C]ethylpyruvate, AH111501 trityl radical, and Dotarem gadolinium chelate contrast agent for DNP[21]. 10μL and 15μL samples of [1-^{13}C]ethylpyruvate were hyperpolarised with OX063 and AH111501 radicals with varying concentrations of gadolinium contrast agent added. These experiments are summarised in Fig. 5, and found that [1-^{13}C]ethylpyruvate hyperpolarisation with AH111501 achieved a higher maximum polarisation at all contrast concentrations than with OX063[84].

However, the utility of [1-^{13}C]ethylpyruvate as a lipophilic neurotracer was established by Hurd *et al*[24], who used the Finland radical in their DNP mixture. I sought to ascertain whether the previously developed AH111501 mixture was superior (shorter build-up time and higher maximum polarisation) to a DNP mixture containing an equivalent concentration of Finland radical at several concentrations of gadolinium contrast agent.

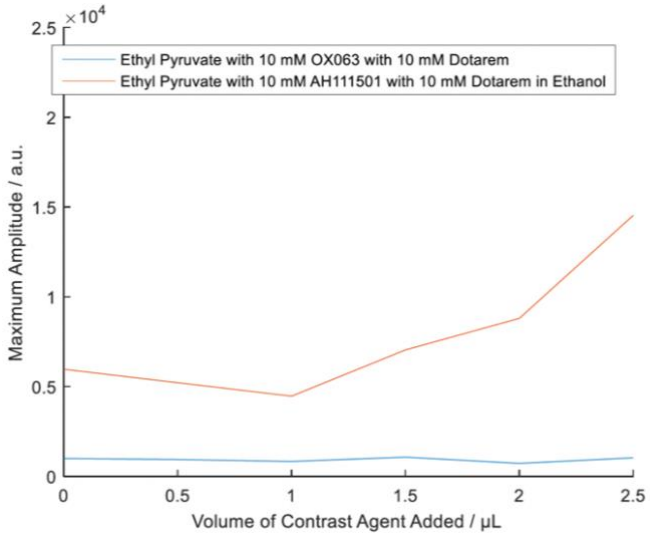


Figure 5. Reproduced from Fisher, 2014[84]. Maximum polarisation amplitude with [1-^{13}C]ethylpyruvate is higher at all Dotarem gadolinium contrast concentrations with AH111501 radical than OX063.

2.2 Methods

2.2.1 Overview

30µL [1-^{13}C]ethylpyruvate samples with two different radicals: AH111501 (Syncom, Best, The Netherlands) and Finland (Merck, Kenilworth, NJ), were hyperpolarised. The volume of Dotarem gadolinium chelate contrast agent (Guerbet Laboratories Ltd, UK) added was varied between 1µL and 5 µL for the Finland radical. Hyperpolarisation was performed using a HyperSense system (Oxford Instruments, Abingdon, UK).

2.2.2 [1-^{13}C]Ethylpyruvate-Finland Radical Sample Preparation

[1-^{13}C]Ethylpyruvate was obtained from Cambridge Isotopes Laboratories, Inc., Tewksbury, MA. [1-^{13}C]Ethylpyruvate was diluted 1:5 volume:volume with neat ethanol. After [1-^{13}C]ethylpyruvate dilution, the solution was doped with 15mM Finland radical[24]. I found that with lower ethanol concentration, dissolution of radical was not possible. After radical addition, 3 x 2-minute rounds

of mixing using a vortex ensured radical dissolution in [1-^{13}C]ethylpyruvate-ethanol solution. A stock solution of Dotarem contrast agent mixed 2:98 volume:volume with neat ethanol was prepared. To 30µL of [1-^{13}C]ethylpyruvate-radical solution was added either 5µL, 2.5µL, or 1µL of Dotarem-ethanol solution, thus forming 5:30, 2.5:30 and 1:30 volume:volume contrast agent:[1-^{13}C]ethylpyruvate samples. Final concentrations of gadolinium were 1.42mM, 0.71mM and 0.36 mM respectively. The resulting solution was then vortexed for a further 2 minutes to ensure adequate mixing. Five build-up monitoring experiments were performed at each gadolinium concentration.

2.2.3 [1-^{13}C]Ethylpyruvate-AH111501 Radical Sample Preparation

[1-^{13}C]Ethylpyruvate-AH111501 samples were prepared as above for Finland radical samples, however [1-^{13}C]Ethylpyruvate was neat doped with 15mM AH111501 radical, and did not require dilution in ethanol before radical addition. To 30µL of [1-^{13}C]ethylpyruvate-radical solution was added 5µL of 2:98 Dotarem:ethanol solution, forming a 5:30 volume:volume contrast agent:[1-^{13}C]ethylpyruvate sample (1.4mM). Five repeat build-up monitoring experiments were performed.

2.2.4 [1-^{13}C]Ethylpyruvate Hyperpolarisation

[1-^{13}C]Ethylpyruvate samples were hyperpolarised using a HyperSense system (Oxford Instruments, Abingdon, UK). A frequency sweep was performed before hyperpolarisation build-up experiments were started with each different radical and contrast agent concentration to determine the optimal microwave irradiation frequency. Frequency sweeps were performed between 94.066 and 94.236 GHz at 0.01 GHz intervals with a 120s irradiation time. An example frequency sweep is shown in Fig. 6, performed on an AH111501 sample. A frequency of 94.102 GHz was selected for hyperpolarisation in this example. A microwave power of 100 mW was used throughout. After optimal microwave frequency was ascertained, each sample was hyperpolarised, with signal monitored every 120s. Hyperpolarisation time varied between ethylpyruvate samples. Samples were

allowed to polarise until they had reached the plateau phase of the build-up curve (range 90 – 220 minutes). 5 replicates were completed in each group, with the exception of the Finland radical group with 1μL of added contrast agent, in which three replicates were obtained.

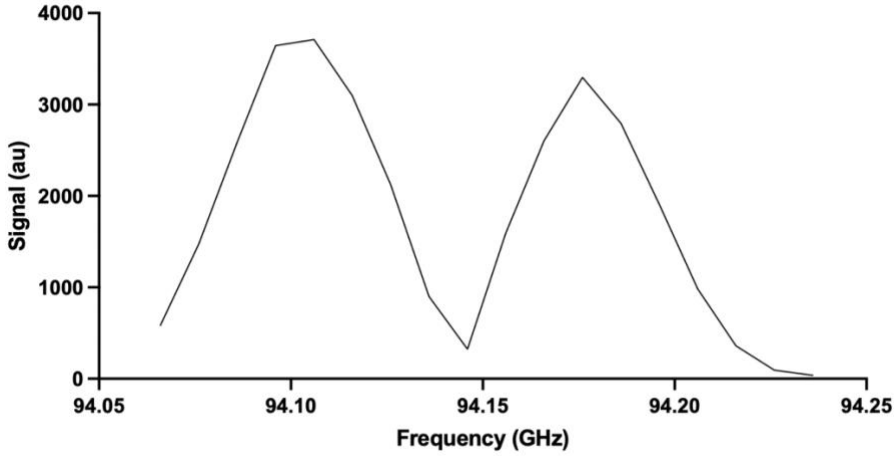


Figure 6. Example frequency sweep using AH111501 radical

2.2.5 Data Fitting and Statistical Analysis

Hyperpolarisation build-up data were fitted using in-built software on the HyperSense system. Statistical analysis of polarisation build-up times and maximum polarisation amplitudes with Finland radical were conducted by a Kruskall-Wallis test with post-hoc Dunn's multiple comparisons. The Finland 2.5:30 group was selected for comparison by Mann Whitney test to AH111501, as of the groups with five data points, it had the highest mean solid state signal amplitude, and shortest average build-up time constant. All statistical tests were performed in GraphPad Prism (version 9.2.0, GraphPad Software Inc., CA, USA). $P<0.05$ assumed for significance.

2.3 Results

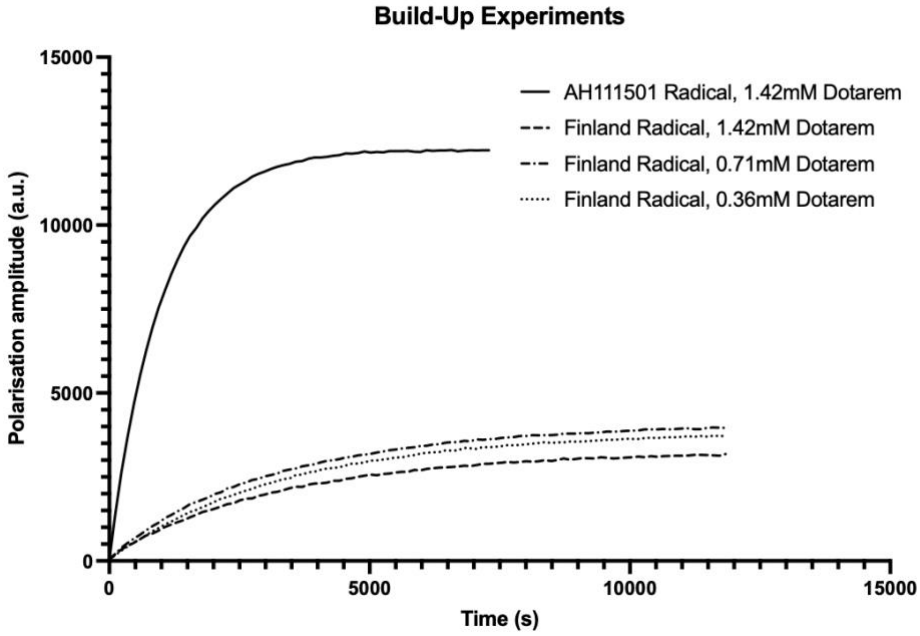


Figure 7. Representative build-up data from each group demonstrating the higher polarisation and shorter build-up time in the AH111501 radical group.

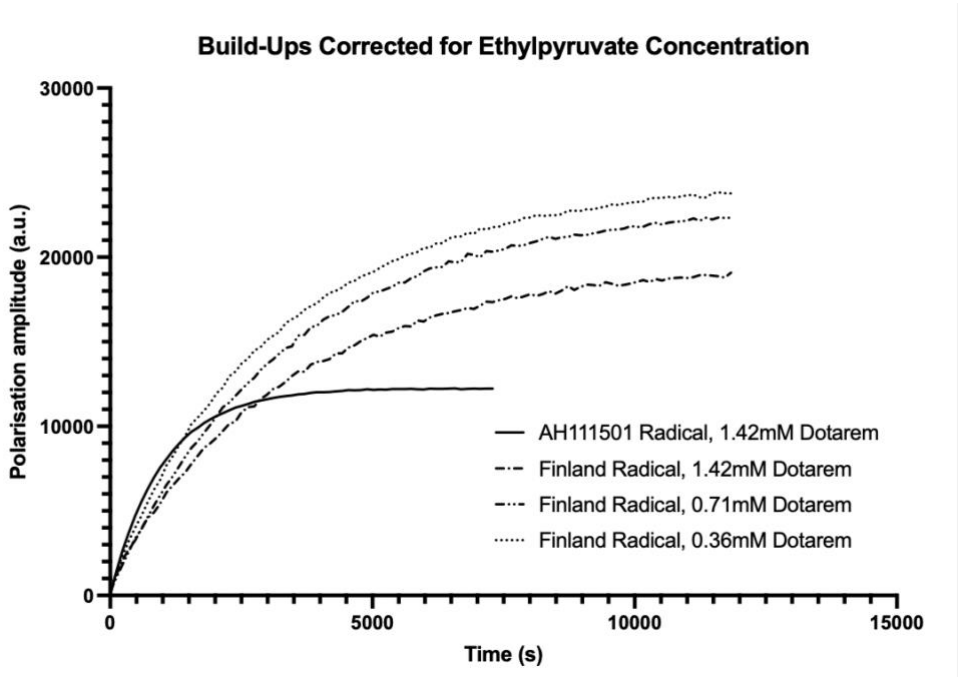


Figure 8. Representative build-up data from each group illustrating greater polarisation with Finland radical when data are corrected for ethylpyruvate concentration. Ethylpyruvate concentration is 6x higher in AH111501 mixture, therefore Finland data has been multiplied by 6 and plotted to correct for ethylpyruvate concentration.

Example data from four representative build-up experiments are shown in Fig. 7, and data corrected for ethylpyruvate concentration are shown in Fig. 8. A summary of build-up time and maximum polarisation values for each radical-contrast mixture can be found in Table 1 and are graphically

represented in Fig. 9. A Kruskall-Wallis test between all Finland radical groups revealed no difference between groups for build-up time (p=0.32). While the Kruskall-Wallis test for maximum polarisation was significant (p=0.05), post-hoc Dunn's tests revealed no significant pairwise comparisons. Build-up time was shorter, and maximum polarisation higher in the AH111501 radical with 5µL added gadolinium chelate group than in the Finland radical with 2.5µL gadolinium chelate group (p=0.008) and p<0.007 respectively).

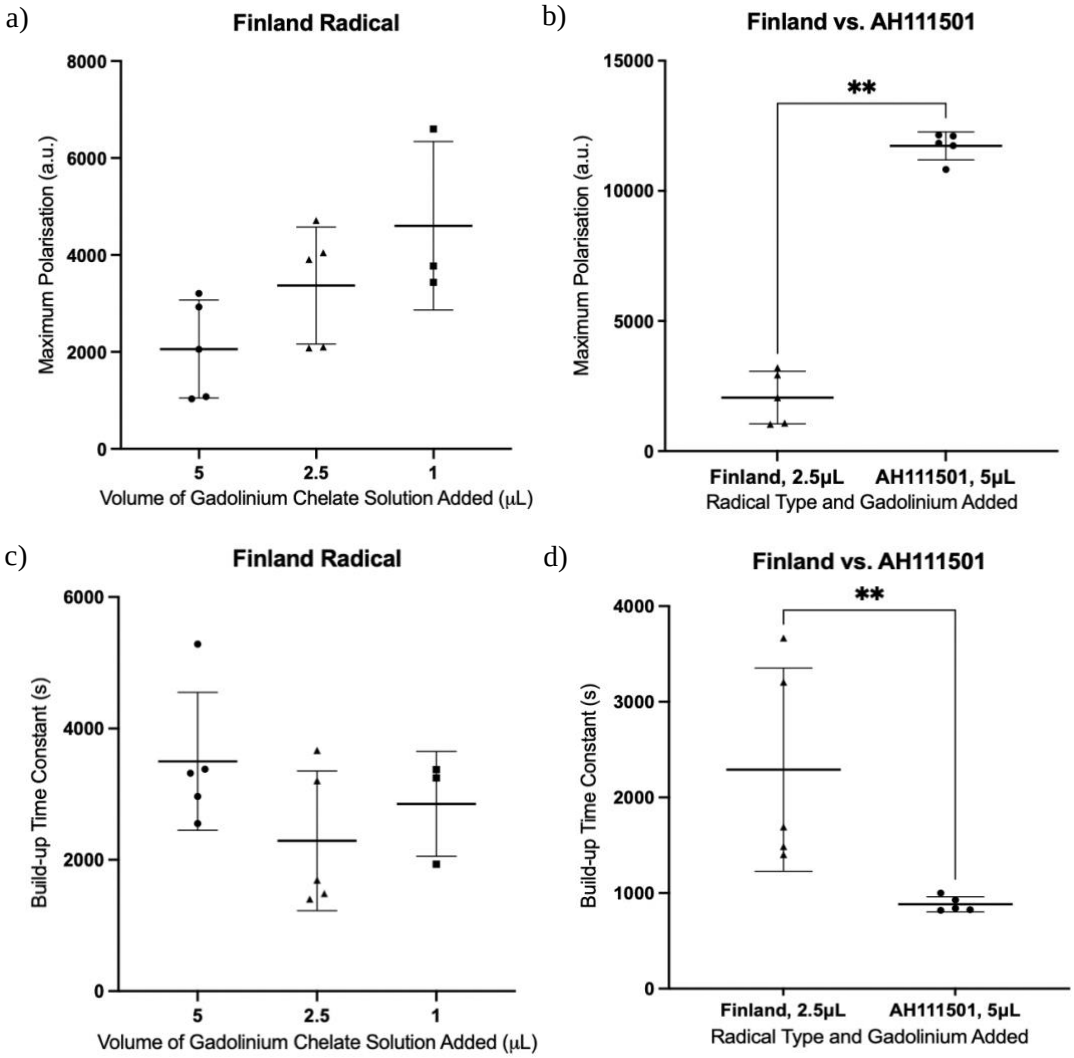


Figure 9. Scatter plots showing the data points, mean and standard deviation of maximum polarisation (a) and build-up time constant (c) data from all Finland radical groups. Comparison of Finland radical with 2.5 µL added gadolinium solution with AH111501 radical for maximum polarisation (b) and build-up time constant (d) data. n = 5 in each group, excepting the Finland group with 1µL added gadolinium solution, where n=3. *p<0.05, **p<0.01, ***p<0.001, ****p<0.0001.

Radical	Gadolinium Concentration / mM	Build-up Time Constant / s	Maximum Signal / au
Finland	1.42	3500 (1051)	2059.2 (1012)
	0.71	2290.6 (1063)**	3369.6 (1205)**
	0.36	1963.4 (1341)	3474.8 (1974)
AH111501	1.42	882.4 (80)	11729.6 (536)

Table 1. Build-up time and maximum polarisation data from build-up experiments displayed as group mean (standard deviation). n = 5 for each group except Finland 0.36mM, where n = 3. *p<0.05, **p<0.01, ***p<0.001, ****p<0.0001 vs. AH111501. All radical concentrations 15mM.

2.4 Discussion

Compared to the Finland radical, [1-^{13}C]ethylpyruvate DNP using AH111501 radical provides a higher maximum polarisation amplitude, and also a shorter build-up time constant, on the order of approximately 900s. This is short enough to allow significant hyperpolarisation during the timeframe of a typical rodent scanning protocol (60-120 mins), allowing hyperpolarised samples for subsequent dissolutions to be ready without waiting for a long period of signal build-up between animals.

Greater overall signal generation with the AH111501 radical is likely due to its solubility in neat ethylpyruvate, rather than an explicit difference in the ability of the two radicals to polarise the sample. As demonstrated above in Fig. 8, the signal generation when corrected for [1-^{13}C]ethylpyruvate concentration was actually higher with the Finland radical, however while Finland radical required ethylpyruvate to be mixed 1:5 volume:volume in ethanol before radical dissolution, AH111501 did not require ethylpyruvate dilution. This results from the more lipophilic nature of the AH111501 radical relative to Finland radical. The basis of [1-^{13}C]ethylpyruvate's usefulness as a neurotracer is dependent upon its lipophilicity, which allows direct diffusion of tracer into the CNS, and as such a lipophilic radical is more soluble in neat [1-^{13}C]ethylpyruvate. Therefore the [1-^{13}C]ethylpyruvate concentration in our AH111501 mixture was approximately six times higher than in the Finland mixture.

In conclusion, AH111501 represents a better radical for [1-^{13}C]ethylpyruvate DNP than Finland due to its lipophilicity, which allows a higher concentration of [1-^{13}C]ethylpyruvate to be maintained in the injected mixture. Comparison of build-up data with different ^{13}C MRS tracer-radical combinations such as those presented here will allow future experiments to effectively manipulate a mixture to produce properties conducive to imaging their specific tissue or area of interest.

Chapter 3 – Optimising an Anaesthetic Protocol for Hyperpolarised ^{13}C Neuroimaging

3.1 Cerebral Oxygen Consumption and Perfusion

Key to drawing appropriate conclusions with metabolic neuroimaging and spectroscopy using an intravenous tracer, are cerebral perfusion and the maintenance of normal physiological cerebral metabolism. The T_1 of the hyperpolarised tracer limits acquisition time to around two minutes or less from the point of injection. Therefore, for the intravenously injected tracer to reach the brain, enter the CNS, and become incorporated into CNS metabolism sufficiently to produce observable metabolic changes, cerebral perfusion must be maintained as far as possible to facilitate bulk transport of the tracer. Furthermore, to make inferences about the changes from normal metabolism seen in disease, underlying physiology must be maintained as close to normal as possible under anaesthesia.

^{13}C imaging and spectroscopy has recently been applied to neuroimaging in several preclinical settings including neuro-oncology[85], stroke[86], traumatic brain injury[87], and MS[23,79]. However, in several hyperpolarised ^{13}C neuroimaging studies, animals have been anaesthetised using isoflurane in 100% O_2[21,79]. At first, the rationale for this – to compensate for presumed hypoventilation under anaesthesia – is clear. However, in the absence of disease and at rest, oxygen uptake is perfusion- rather than diffusion-limited[88], and in rats, it has been shown that the cerebral metabolic rate of oxygen consumption ($CMRO_2$) is maintained until very low arterial oxygen tension[89]. Therefore, the relative hypoventilation expected in anaesthetised animals is unlikely to result in any profound central hypoxia or reduction in cerebral oxidative metabolism.

On the contrary, there is evidence that over-oxygenation may have detrimental effects on both cerebral perfusion and normal cerebral metabolism. It has been demonstrated that in rats, cerebral blood flow (CBF) is reduced under hyperoxic conditions[90], and conversely that CBF and cerebral blood volume (CBV) are increased by hypoxia[89]. This effect has been observed in several species, and with the advent of non-invasive MR techniques for assessment of CBF and CBV in humans, has been demonstrated in man as well[91–93]. The mechanism by which hyperoxia induces cerebral vasoconstriction has not yet been fully elucidated. It has been demonstrated that raised carbon dioxide tension is a potent vasodilatory stimulus[94]. One theory proposed is that with increased oxygen tension, oxygen displaces carbon dioxide from haemoglobin binding sites, reducing total blood carbon dioxide content and carbon dioxide-mediated vasodilation, however this effect is thought to be too small on its own to be responsible for hyperoxic vasoconstriction[95]. Instead, it has been suggested that hyperoxia disturbs the balance of reactive oxygen and nitrogen species (ROS and RNS). Superoxide anions react with nitric oxide (NO) to produce RNS in a rection catalysed by superoxide dismutase 3 (SOD3). Under physiological conditions, NO is a key cerebrovasodilator. With increased superoxide availability under hyperoxic conditions, it is possible that SOD-catalysed conversion of NO to $ONOO^-$ RNS depletes the pool of NO, and removes tonic NO vasodilation, resulting in cerebral vasoconstriction[96].

While there is a lot of data regarding the cerebrovascular effects of changes in inspired oxygen concentration, less data is available regarding cerebral metabolism, particularly under hyperoxic conditions. Examination of hyperoxia is usually performed in the context of potential hyperoxic therapy for stroke and TBI, and therefore takes place under non-physiological conditions in stroke or TBI models. Partly, the lack of metabolic data has been due to the technical difficulty of calculating the usual metrics used to denote cerebral metabolic rate: $CMRO_2$, which relies on the Fick principle (CBF x arterial O_2 – venous O_2), and the oxygen extraction fraction (OEF) (arterial O_2 – venous O_2/arterial O_2)[97]. Until recently, both necessitated serial arterial and venous blood sampling, however advances in MR have allowed non-invasive arterial and venous oxygen quantification[98]. Using this technique, Xu *et al*. showed that $CMRO_2$ is reduced in humans under

hyperoxic conditions. This is corroborated by findings from the reverse experiment, which demonstrated increased $CMRO_2$ under hypoxic conditions[92]. These newer MR techniques have largely been applied in human studies, which do not require anaesthesia, in which it is easy to identify the large vascular structures used in calculations, and which are directly applicable to clinical practice, without the need for translation of results from animal models. However, using blood oxygen level dependence (BOLD) MR in rats, Lu *et al*. identified 'superfluous oxygenation throughout the brain' under hyperoxic challenge[90]. Beyond effecting cerebrovascular changes as described above, ROS may induce oxidative stress in the cerebral tissue itself[97], which may account for the hyperoxic drop in $CMRO_2$. Noseworth and Bray, using Gd-enhanced proton MRI and ^{31}P MRS in rats after exposure to 85% inspired oxygen, noted increased BBB permeability and an increase in high-energy phosphate levels. The authors hypothesised that oxidative stress forced cells to upregulate ATP production in order to deal with the structural and metabolic damage done by ROS[99]. Corroborating this, histological analysis of segments of the rat medullary caudal solitary complex after euthanasia under normobaric hyperoxic conditions revealed supraphysiological levels of ROS and RNS[100]. Studies conducted in newborn piglets found that tyrosine and serine residues in key anti-apoptotic mitochondrial proteins were phosphorylated after hyperoxic exposure, while pro-apoptotic proteins were not, suggesting a mechanism by which hyperoxia may induce cell death[101,102]. Likewise, mice exposed to mild hyperoxia (30% inspired O_2) over a 28-day period developed evidence of oxidative damage of a comparable degree to that seen after 28 days of hypoxia (10% inspired O_2)[103]. This hyperoxic increase in oxidative stress is increasingly being recognised in clinical medicine. In critical and perioperative care, it is common to pre-oxygenate patients with 100% inspired O_2 to buffer against apnoeic periods during intubation and extubation. However, hyperoxia is recognised as an independent mortality risk factor in critically ill patients, and there is some controversy in the field as to the benefits of pre-oxygenation, given the almost total saturation of haemoglobin at physiological inspired oxygen tensions[104].

In summary, there is evidence that both cerebral blood flow and cerebral metabolism are directly affected by hyperoxia, and that therefore development of an anaesthetic protocol which promotes

physiological cerebral perfusion and metabolism will be beneficial not only in rapid delivery of our neurotracer to the brain, but in the confidence with which we may extrapolate from an anaesthetised rat model to metabolism in awake humans.

Here, I have used perfusion MRI and hyperpolarised [1-^{13}C]pyruvate spectroscopy to compare cerebral perfusion and basal metabolism under anaesthesia in a sample group of three rats, each imaged at 100%, 90% and 60% inspired O_2, with the remainder of inspired gas made up with N_2O. N_2O is an analgesic gas commonly used alongside an anaesthetic during animal anaesthesia, and is vasoactive in and of itself. In both rats and humans N_2O has been shown to increase CBF, but does not appear to independently affect $CMRO_2$[105,106].

3.2 Methods

3.2.1 Overview

Three female Wistar rats were each serially anaesthetised and imaged with proton perfusion MRI and [1-^{13}C]pyruvate MRS at three different inspired oxygen concentrations, in order to assess the effect of inspired oxygen concentration on cerebral perfusion and metabolism under anaesthesia.

3.2.2 Animal Handling

Experiments were performed on three female Wistar rats aged 10 weeks at the time of purchase (Charles River, Wilmington, MA). Rats had access to water *ad libitum* and were housed together with allergen-free bedding. Ethical approval was granted following review by both the University of Oxford Clinical Medicine Ethical Review Committee, and as part of the project license application. All animal experiments and procedures were performed out with the appropriate personal, project and institutional licences granted under the UK Animals (Scientific Procedures) Act 1986. All experiments were conducted in accordance with the University of Oxford Policy on the Use of Animals in Scientific Research.

3.2.3 Anaesthetic Protocol

Anaesthesia was induced using an anaesthetic induction box at 2.5% isoflurane and the inspired gas mixture used throughout the rest of the experiment. Following induction, anaesthesia was maintained with 2% isoflurane throughout. Animals were weighed, and tail vein cannulation was performed before transfer to a home-made scanning cradle with a 2-channel surface receive coil (Rapid Biomedical, Rimpar). Anaesthesia was maintained during scanning by positioning of the nose within a built-in nose cone. Inspired oxygen concentration was varied, and oxygen was replaced by N_2O in the inhaled mixture. Each rat was anaesthetised three times, with scanning performed at 100% O_2, 90%:10% O_2:N_2O, and 60%:40% O_2:N_2O. At least 1 week of recovery time was allowed between scans. Permanent pen was used to mark the brain prior to each scan to allow optimal positioning within the cradle.

3.2.4 [1-^{13}C]Pyruvate MRS

[1-^{13}C]Pyruvate (Sigma-Aldrich, Gillingham, UK) was neat-doped with 15mM of OX063 trityl radical (Merck, Kenilworth, NJ). A stock solution of Dotarem gadolinium chelate solution diluted 1:50 volume:volume with ddH_2O was prepared. 3µL of 1:50 Dotarem was added to each 30µL sample of [1-^{13}C]pyruvate.

Hyperpolarised [1-^{13}C]pyruvate was prepared by 1 hour of hyperpolarisation at ~1 K (prototype polariser, 3.35 T) as described by Ardenkjaer-Larsen *et al*[16] before being rapidly dissolved in 4.5 mL of pressurised, heated sodium hydroxide solution. This produced a solution of 80mM hyperpolarised sodium [1-^{13}C]pyruvate at physiological temperature and pH, with a polarisation of ~20%. One millilitre of this solution was injected over 2 seconds via a tail vein cannula (dose of ~0.32 mmol/kg) with a 300 µL saline flush.

Initial localiser images acquired using a ^{1}H/^{13}C volume transmit/receive coil and a 3D gradient echo sequence (TR = 5ms, TE = 1ms**,** flip angle = 10°, RF spoiled, FOV = 60mm^3, acquisition matrix =

256 x 256 x 64, reconstruction matrix = 512 x 512 x 64). After localiser images were acquired, a 2D multi-echo B_0 mapping sequence was performed with subsequent automated shimming.

Hyperpolarised [1-^{13}C]pyruvate spectroscopy was performed using a pulse-acquire sequence (excitation pulse = sinc, excitation pulse width = 500µs, TR = 1s, TE = 0.3ms, slice thickness = 20mm, flip angle 15º, number of time points = 240) using a 2-channel ^{13}C surface array coil and ^{1}H/^{13}C quadrature volume transmit coil. The spectroscopic slice encoding slab covered the whole brain in coronal orientation.

3.2.5 Perfusion Weighted MRI

After [1-^{13}C]pyruvate MRS, rats were transferred whilst anaesthetised to a dedicated neuro-imaging cradle with a 4-channel ^{1}H array (Rapid Biomedical, Rimpar, Ger) placed over the brain with bite bar and ear pins for consistent positioning. As above, a 3D gradient echo localiser sequence was performed and B_0 shimming applied. Dynamic susceptibility contrast (DSC) perfusion MRI (Dotarem gadolinium bolus = 200µL, 300µL saline flush, TE = 10ms, TR = 20ms, flip angle = 20°, FOV = 35mm, acquisition matrix = 128 x 64, number of slices = 1, slice thickness = 0.625mm, number of time points = 60, time resolution = 1s) was performed.

3.2.6 [1-^{13}C]Pyruvate MRS Processing

Spectra from each channel were summed separately in the frequency domain and combined after phasing. Spectra were fit in jMRUI (MRUI Consortium) assuming [1-^{13}C]pyruvate, [1-^{13}C]pyruvate hydrate, [1-^{13}C]lactate, [1-^{13}C]alanine, and [1-^{13}C]bicarbonate as basis functions. Cramer Rao lower bound (CRLB) and mean signal for each metabolite was recorded. Lactate:total carbon, bicarbonate:total carbon, and bicarbonate:lactate ratios were calculated per rat, per gas mixture. Pyruvate, lactate, and Bicarbonate signal to noise ratios (SNR) were calculated as the peak summed amplitude of the respective metabolite peak divided by the standard deviation of the last 100 points in the Free Induction Decay.

3.2.7 DSC MRI Processing

Perfusion weighted imaging post-processing was performed using model-free deconvolution. A region of interest was placed in the supplying vessels to determine an arterial input function (AIF), and used to generate CBV, CBF, time to peak (TTP), and mean transit time (MTT) maps[107]. A region of interest was drawn to encompass the whole brain and mean values for each quantity calculated.

3.2.8 Statistical Analysis

All data was assumed to be non-normally distributed. Friedman's test was used to assess for group-wise differences over gas conditions in weight, metabolite, CRLB, SNR, CBF, CBV, TTP and MTT, and metabolic ratios. Wilcoxon signed rank tests were used for post-hoc analysis with Bonferroni correction. Spearman's correlation was used to assess for correlations between metabolic and perfusion parameters. $P<0.05$ assumed to be significant. All statistical tests were performed in R. Power calculations were conducted for perfusion parameters using standard formulae[108], a significance criterion of $p<0.01$, and 90% statistical power.

3.3 Results

3.3.1 Perfusion MRI

	Inspired Mixture (O_2:N_2O)		
	100:0	**90:10**	**60:40**
Weight (g)	250 ± 9	265 ± 10	268 ± 8
CBF (mL/100g/min)	60 ± 19	109 ± 35	106 ± 23
CBV (mL/100g)	0.91 ± 0.35	1.34 ± 0.68	0.8 ± 0.27
MTT (s)	0.93 ± 0.17	0.78 ± 0.22	0.49 ± 0.07
TTP (s)	8.3 ± 1.2	7.7 ± 0.9	6.3 ± 0.8

Table 2. Summary of proton MRI data with varying inspired oxygen concentration. Values stated as mean ± SD. CBF = cerebral blood flow, CBV = cerebral blood volume, MTT = mean transit time, TTP = time to peak.

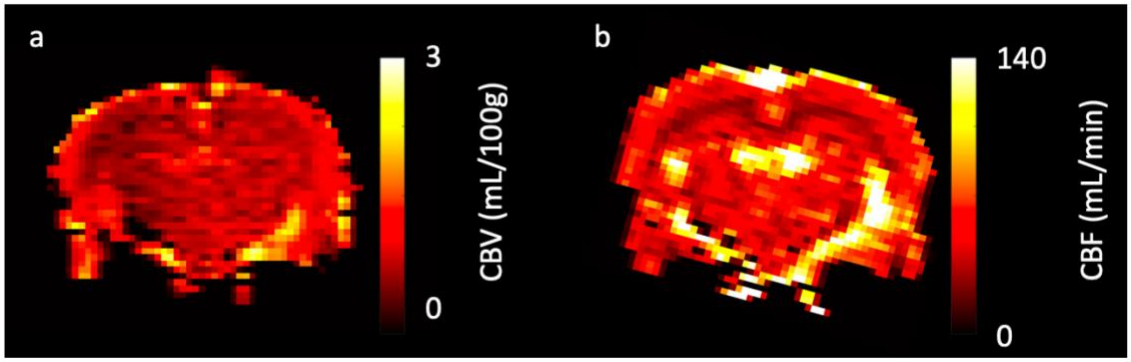


Figure 10. Example CBV and CBF maps at 60:40 O_2:N2O.

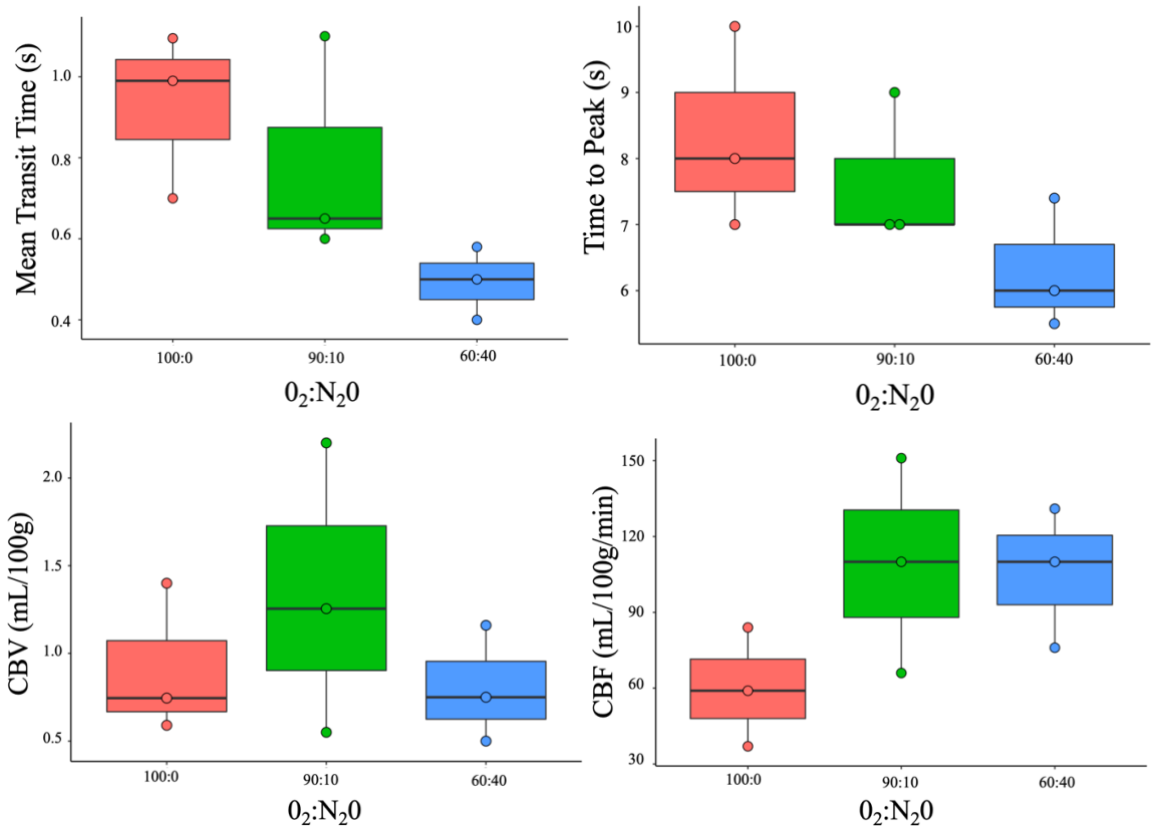


Figure 11. A trend towards increased CBF, and reduced MTT and TTP at lower inspired oxygen concentrations. Perfusion MRI data showing MTT, TTP, CBV and CBF at 100:0, 90:10 and 60:40 O_2:N_2O. CBF = cerebral blood flow, CBV = cerebral blood volume, MTT = mean transit time, TTP = time to peak. n=3.

DSC perfusion MRI data were collected in three rats at three inspired oxygen concentrations. MTT, TTP, CBV and CBF maps were calculated. Data is summarised in Table 2. Example CBV and CBF maps are shown in Fig. 10. No effect of weight was found between groups (p=0.21). Friedmann's tests were performed for MTT, TTP, CBV and CBF to test for differences between inspired oxygen mixtures, and no differences were identified. However, as illustrated in Fig. 11, there was a trend

towards reduced MTT (p = 0.09), reduced TTP (p=0.25), and increased CBF (p=0.20) with reduced inspired O_2 concentration and increased inspired N_2O. No trend was observed with CBV and inspired gas mixture (p=0.52). After correction for multiple comparisons, Spearman's test revealed a correlation between CBV and CBF (p=0.01). There were no other correlations.

3.3.2 Hyperpolarised [1-^{13}C]Pyruvate MRS

	Inspired Mixture (O_2:N_2O)		
	100:0	**90:10**	**60:40**
Weight (g)	250 ± 9	265 ± 10	268 ± 8
Lactate:Total Carbon Ratio	0.090 ± 0.02	0.14 ± 0.02	0.131 ± 0.01
Bicarbonate:Total Carbon Ratio	0.012 ± 0.003	0.016 ± 0.01	0.03 ± 0.01**††
Bicarbonate:Lactate Ratio	0.12 ± 0.01	0.11 ± 0.01	0.25 ± 0.07**
Pyruvate CRLB (%)	4.0 ± 1.0	3.9 ± 0.9	1.2 ± 0.2*
Lactate CRLB (%)	18 ± 4	14 ± 1	6 ± 1*†
Bicarbonate CRLB (%)	239 ± 175	58 ± 23	16 ± 1**†
Pyruvate SNR	26.3 ± 7.9	26.5 ± 4.6	82.4 ± 11.9*†
Lactate SNR	5.9 ± 1.3	7.0 ± 0.6	18.4 ± 4.6*†
Bicarbonate SNR	0.7 ± 0.4	0.76 ± 0.1	6.2 ± 2.6*†

Table 3. Summary of [1-^{13}C]ethylpyruvate MRS data with varying inspired oxygen concentration. Values stated as mean ± SD. CRLB = Cramer Rao lower bound. n=3. *p<0.05, **p<0.01, ***p<0.001, ****p<0.0001 vs 100% inspired O_2. †p<0.05, ††p< 0.01, †††p<0.001 vs 90:10 O_2:N_2O.

Hyperpolarised [1-^{13}C]pyruvate MRS using a whole-brain slice was performed serially on three female Wistar rats at three inspired oxygen concentrations. Lactate and bicarbonate peaks from summed spectra were normalised to total carbon signal, and directly compared to each other. Example summed spectra can be seen in Fig. 12.

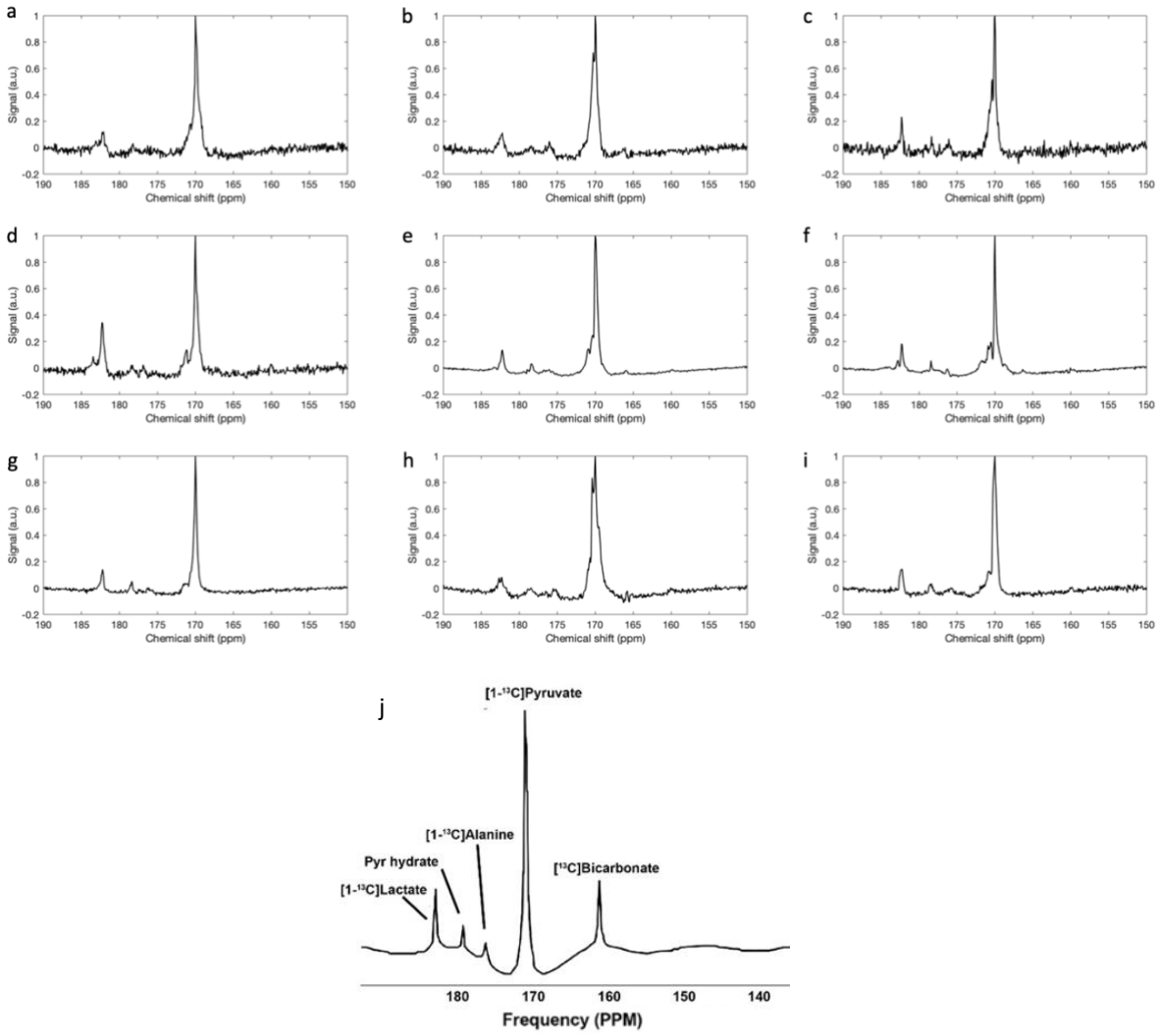


Figure 12. Summed spectra from cerebral [1-^{13}C]pyruvate spectroscopy in 3 rats at 100% O_2 (a-c), 90:10 O_2:N_2O (d-f), and 60:40 O_2:N_2O (g-i). Spectra normalised to peak pyruvate, and shown with no line broadening. (j) Reproduced from Lewis *et al*. 2020 Clinical Cardiovascular Applications of Hyperpolarised Magnetic Resonance, showing example pyruvate spectrum with labelled metabolite peaks.

Visually comparing summed spectra at 100% O_2 (Fig. 12a-c) to that at 90:10 and 60:40 O_2:N_2O (Fig. 12d-f and 12g-i), a bicarbonate peak is barely visible at 100% O_2 but is visible at lower O_2 concentrations. Further, there is a larger amount of noise visible in the baseline of Fig. 12a-c than Fig. 12d-f or 12g-i. No difference in lactate:total carbon ratio was observed between the inspired oxygen mixtures, however, though difficult to appreciate on simple inspection of the spectra in Fig. 12, quantitative spectral analysis revealed a trend towards decreased lactate:total carbon ratio at 100% O_2 ($p=0.07$, Fig. 13a). Friedman's test revealed a difference in bicarbonate:total carbon ratio between groups ($p=0.002$). Bicarbonate:total carbon ratio was increased at 60:40 O_2:N_2O versus both 100% inspired O_2 ($p=0.003$) and 90:10 O_2:N_2O ($p=0.007$) (Fig. 13b). The bicarbonate:lactate

ratio was also different between inspired oxygen concentrations (p=0.03). Bicarbonate:lactate ratio was higher at 60:40 O_2:N_2O than at 100% O_2 (p=0.01).

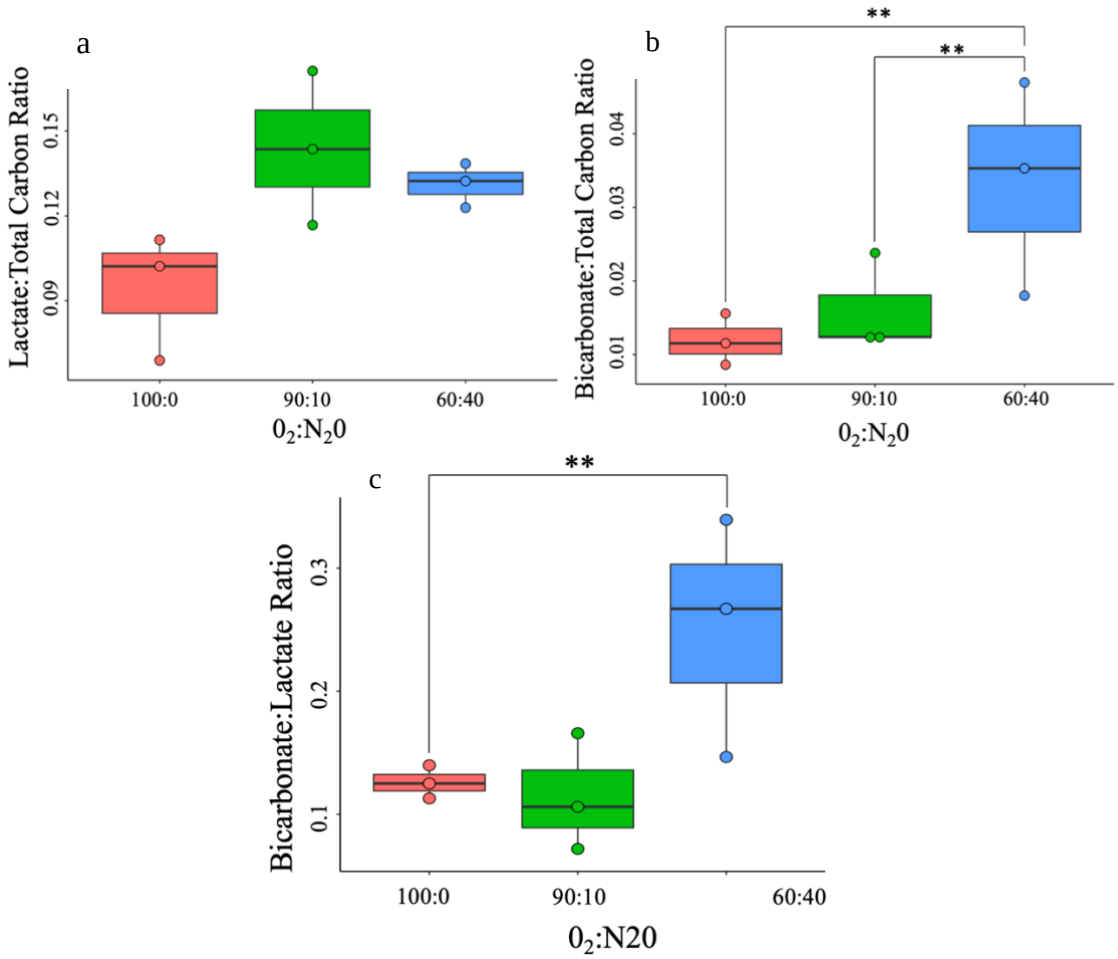


Figure 13. Changes in inspired oxygen concentration alter cerebral lactate and bicarbonate production. Hyperpolarised [1-^{13}C]pyruvate MRS data showing cerebral lactate:total carbon (a), bicarbonate:total carbon (b) and bicarbonate:lactate (c) ratios compared at varying inspired oxygen concentrations. n=3. *p<0.05, **p<0.01.

The SNR and CRLB was calculated for bicarbonate, lactate and pyruvate spectroscopic peaks, and compared between inspired oxygen concentrations. This data is summarised in table 3, and figures 14 and 15. The CRLB for pyruvate was reduced at 60:40 O_2:N_2O compared to 100% O_2 (p=0.03), and almost reached significance versus 90:10 O_2:N_2O (p=0.05). CRLB was lower at 60:40 O_2:N_2O than both 100% O_2 (p=0.01) and 90:10 O_2:N_2O (p=0.04) for lactate. The mean CRLB for bicarbonate was 239% at 100% O_2 and was higher than in the 60:40 O_2:N_2O group (p=0.01). CRLB was also higher in the 90:10 O_2:N_2O group versus 60:40 O_2:N_2O (p=0.03). Likewise, the SNR was higher at 60:40 O_2:N_2O than for either of the other inspired gas mixtures for all metabolites.

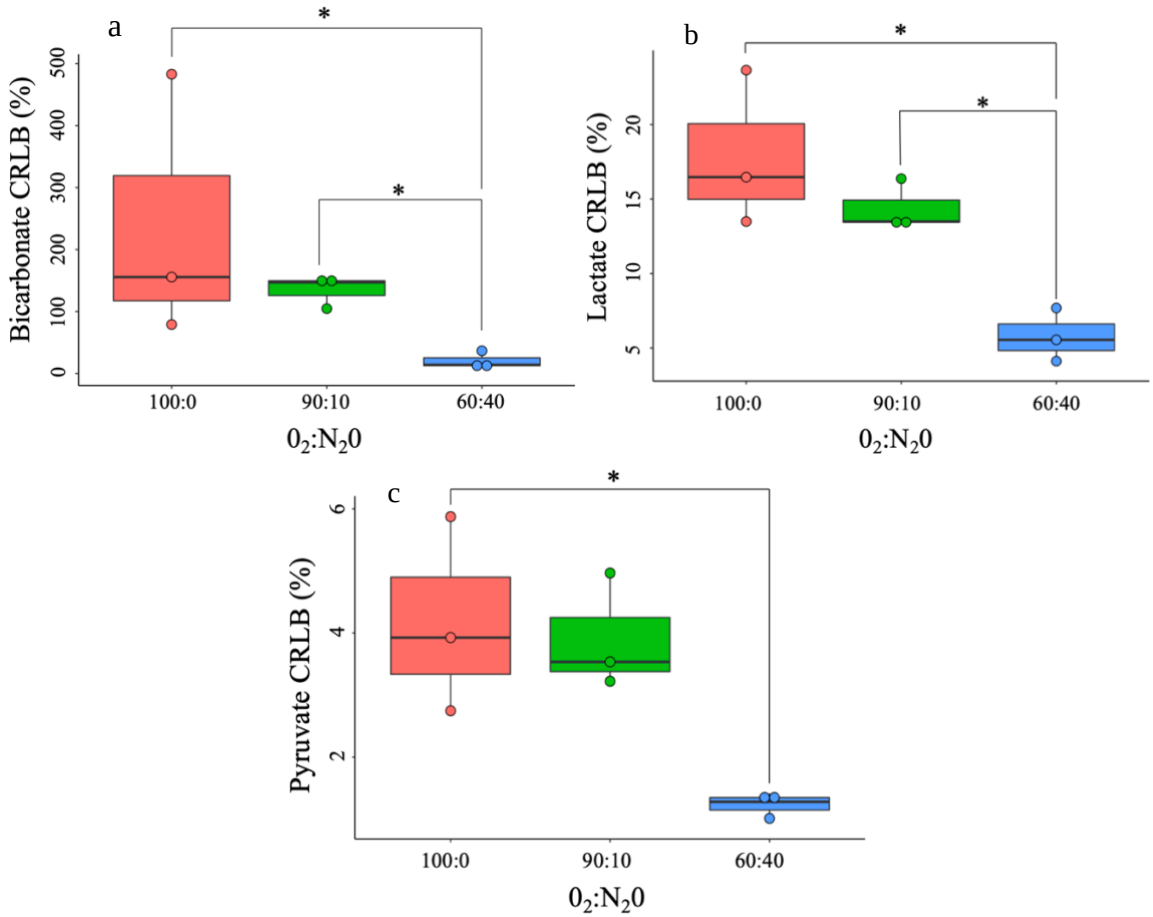


Figure 14. CRLB is reduced for all metabolites at lower inspired oxygen concentration. Cramer rao lower bound data for cerebral bicarbonate (a), lactate (b), and pyruvate (c) [1-^{13}C]pyruvate spectroscopy data. n=3. * = $p<0.05$.

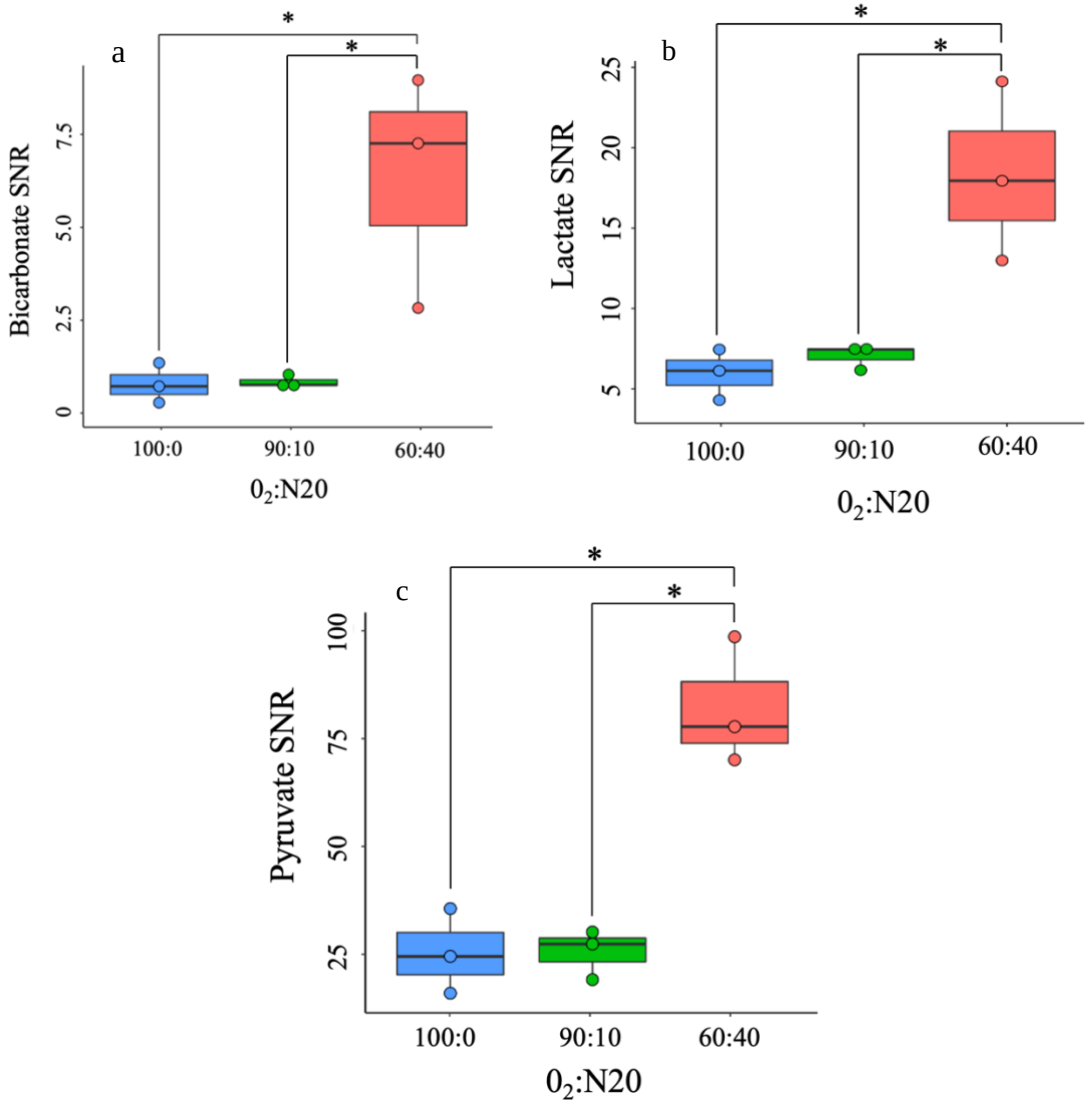


Figure 15. SNR is increased for all metabolites at lower inspired oxygen concentration. SNR data for cerebral bicarbonate (a), lactate (b), and pyruvate (c) [1-^{13}C]pyruvate spectroscopy data. n=3. * = $p<0.05$

3.4 Discussion

3.4.1 Hyperoxia Reduces Cerebral Perfusion

Our results did not identify a difference between measures of cerebral perfusion at different inspired oxygen concentrations, however several trends were revealed. CBV appeared to increase at 90:10 O_2:N_2O relative to the two other inspired gas mixtures. This trend appears to have been driven by a single data point which is markedly higher than any other measurement in any of the three groups. With an n number of only 3 in each group, this study is significantly underpowered and is affected greatly by individual outliers. This apparent trend is likely to represent normal variation rather than a true effect, however repetition with a larger sample size is required before an accurate assessment

can be made. Measurements of CBF, MTT and TTP suggested increased cerebral perfusion with lower inspired oxygen concentration. While CBF measures the amount of blood flowing through cerebral tissue per unit weight per unit time, MTT and TTP represent slightly different characteristics. Decreased TTP at 60:40 O_2:N_2O compared to higher inspired oxygen concentrations demonstrates that an injected bolus (in this case gadolinium contrast agent) reaches the brain more rapidly with lower inspired oxygen, and higher inspired N_2O concentrations. As explained above, given the limited time after dissolution for which hyperpolarised ^{13}C MR signal persists, tracers must be delivered as rapidly as possible to cross the BBB, enter metabolism, and provide as much biochemical data as possible before signal relaxes.

Power calculations revealed that an n of 13 would be required for CBF, TTP and MTT measurements to achieve significance. Repeating this experiment with larger sample sizes would allow us to make reliable recommendations regarding changes which could be made to our existing anaesthetic protocols for rat neuroimaging in future, to ensure that neurotracers are employed to best effect by maximising cerebral perfusion and rate of tracer delivery to the brain. However, given the trends seen in our data it is likely that our experiment would yield data in line with previous experiments[89–93], which suggest a negative correlation between hyperoxia and cerebral perfusion.

A proportion of the changes in cerebral perfusion demonstrated here are likely due not only to the vasoconstrictive effect of hyperoxia, but the vasodilatory effect of NO which will be more abundant with higher inspired N_2O concentrations. It is not possible to pick apart the individual contributions of varying oxygen and NO with only the data presented here. In future, it would be interesting to perform further experiments in which N_2O is held constant, and the remainder of the inspired mixture is substituted for a non-vasoactive gas, for example nitrogen, to isolate the effect of O_2 concentration on cerebral perfusion.

3.4.2 Hyperoxia and Baseline Cerebral Metabolism

Under physiological conditions, the brain utilises aerobic respiration for energy generation[109]. As explained in Chapter 1.6, aerobic respiration via the TCA cycle and oxidative phosphorylation generates CO_2, which is in equilibrium with bicarbonate. Therefore, using hyperpolarised [1-^{13}C]pyruvate MRS under normal physiological conditions, one would expect to observe a bicarbonate peak representing the products of TCA cycle activity[14]. Further, proton MRS studies have demonstrated a steady state lactate level of 0.6-1.0 mM in the healthy human brain[110], and this would be expected to be detected by ^{13}C MRS as well. However, were ATP generation to be increased through oxidative phosphorylation, the size of the bicarbonate peak relative to total carbon signal would be expected to increase, while lactate signal would be expected to remain stable or be reduced. In summary, using hyperpolarised [1-^{13}C] MRS, bicarbonate:total carbon ratio gives a proxy measure for the rate of aerobic respiration, while the lactate:total carbon ratio would be expected to rise, and the bicarbonate:lactate ratio to fall, under anaerobic conditions, in which glycolytic rate is increased, and lactate is produced rather than pyruvate entering the link reaction and TCA cycle.

These data demonstrate a higher bicarbonate:total carbon ratio and bicarbonate:lactate ratio at 60:40 O_2:N_2O than at 100% inspired O_2. Based on the predictions above, this suggests that with lower inspired O_2 concentration, the rate of aerobic oxidative phosphorylation paradoxically increases relative to that under hyperoxic conditions.

There are two competing explanations for these metabolic changes. One is that hyperoxia reduces cerebral perfusion to such an extent that the oxygen demand of the brain is not met, causing a shift towards anaerobic metabolism, increasing lactate production, and reducing bicarbonate production. The other is that hyperoxia induces cerebral oxidative damage, which is responsible for a fall in the rate of oxidative phosphorylation. The effects of changing inspired oxygen concentration on cerebral perfusion have been discussed above. Although this experiment does not allow us to assess the individual contributions of O_2 and NO to cerebral vasoconstriction under hyperoxia, it is clear

that our hyperoxic inspired gas mixture was associated with a degree of cerebral vasoconstriction. However, given that under hypoxic conditions $CMRO_2$ does not begin to fall significantly until extremely low oxygen tensions are reached[89], it is unlikely that vasoconstriction is severe enough to precipitate the observed switch towards anaerobic metabolism. More likely is that hyperoxia results in the generation of ROS, which damage and inhibit the function of mitochondrial proteins, including the machinery of oxidative phosphorylation[97], resulting in reduced TCA cycle turnover and a switch towards anaerobic respiration. Lastly, it is important to consider that hyperoxia-induced cerebral vasoconstriction may prevent sufficient tracer from reaching the brain to make an accurate assessment of metabolite ratios at every high inspired oxygen concentrations. The delivery of larger volumes of tracer to the brain at lower inspired O_2 may in and of itself affect the measured metabolite ratios.

Even if these metabolic data allow us to conclude that hyperoxia under anaesthesia produces a switch away from aerobic towards anaerobic cerebral metabolism, to the author's knowledge, there is currently no way to measure $CMRO_2$ in awake rats, and therefore it is difficult to accurately characterise 'normal metabolism' without interference from anaesthesia. It is instead possible to make inferences about deranged metabolism from the biochemical data presented here, and from comparison to human studies, in which cerebral metabolic rate was elevated during hypoxia[92], and decreased during hyperoxia[97]. Preliminary studies in awake humans using hyperpolarised [1-^{13}C]pyruvate MRI have already been conducted[111], and have reported bicarbonate:lactate ratios for whole brain, white matter, grey matter, and other regions of interest. The quoted value for whole brain bicarbonate:lactate ratio in Grist *et al.*[111] is 0.32 ± 0.15, which we may use as an estimate for the 'normal' bicarbonate:lactate ratio in an awake human. In our study, we found that bicarbonate:lactate ratio was 0.12 ± 0.01 at 100% inspired O_2, 0.11 ± 0.01 at 90:10 O_2:N_2O, and 0.25 ± 0.07 at 60:40 O_2:N_2O. Only at the lower, 60:40 O_2:N_2O inspired mixture does bicarbonate:lactate ratio fall within the range presented by Grist *et al.* in humans. With only 4 patients included in Grist *et al.*'s study, and only three rats imaged here, more data is required to determine a definitive 'normal' range for bicarbonate:lactate ratio, and caution must be exercised

when extrapolating between species, however these studies demonstrate in principle how physiological bicarbonate:lactate ratio could be approximated and used to titrate inspired oxygen concentration under anaesthesia for future metabolic neuroimaging studies.

The data presented in Fig. 14 report the CRLB for the pyruvate, lactate and bicarbonate peaks in our summed spectra at each inspired oxygen concentration. The CRLB, is an expression of our confidence in the fitting of our spectra. A CRLB of 100% indicates that the SD of data points within that set is equal to 100% of the mean of that data set. The lower the CRLB, the higher the confidence in the fitting of a metabolite peak. For pyruvate, CRLB was relatively low, at or below 4% in each group, indicating high confidence in the fitting of our peaks with each inspired gas mixture. Even so, at 60:40 O_2:N_2O, CRLB was lower than at 100% inspired oxygen. A similar trend was borne out when examining lactate measurements. Though the CRLB for each metabolite was less than 20%, 60:40 O_2:N_2O provided a lower CRLB than either higher oxygen concentration, indicating that with lower inspired oxygen, confidence in the data generated increases. The difference in CRLB was most stark when examining the fitting of bicarbonate peaks. The CRLB for bicarbonate at 60:40 O_2:N_2O was 16% ± 1%, however at 100% O_2, the CRLB was 239% ± 175%. The SNR data presented in Fig. 15 corroborate our CRLB calculations. For each metabolite, a higher SNR was obtained at 60:40 O_2:N_2O than at either other inspired gas mixture. This indicates that under hyperoxic conditions, spectroscopic data gathered from measurement of bicarbonate is extremely unreliable, but that fitting is improved at lower inspired oxygen concentration. It must be emphasised that the extremely high CRLB and low SNR at high inspired O_2 concentrations means that the spectroscopic data presented here must be treated with caution when drawing conclusions about biochemical shifts between different inspired gas mixtures.

In addition to the limits low SNR under hyperoxia imposes on our interpretation of biochemical data, this study has several limitations. First, as a preliminary study the number of rats imaged was low at only three. Future work would likely require larger animal cohorts, as demonstrated by the power calculations presented in section 3.4.1. Other considerations include the applicability of our

results to other rat types. Here our experiments were with healthy Wistar rats, however data may need to be corroborated in other rat types, for example Lewis rats which are used in the creation of our model of MS in Chapter 4. More broadly, similar experiments may need to be conducted in other commonly used preclinical species such as mice. Finally, the range of inspired oxygen concentrations covered here is relatively narrow. Due to time constraints and availability of MR equipment, I have presented data from all three inspired oxygen concentrations tested so far. This experiment will be completed by imaging under a 40:60 O_2:N_2O inspired gas mixture, and under anaesthesia with medical air in order to track trends at lower inspired oxygen concentrations.

3.4.3 Conclusion

Taken together, the data presented here suggest reduced cerebral perfusion, and a switch towards anaerobic metabolism with hyperoxia under anaesthesia. In future metabolic neuroimaging studies, a lower inspired oxygen concentration should be considered in order to facilitate rapid transport of tracer to the brain, to allow metabolic measurements to be made on a background of cerebral metabolism as close as possible to normal physiology, and to maximise confidence in the fitting of spectroscopic data.

Chapter 4 – Hyperpolarised [1-^{13}C]Ethylpyruvate MRS as a Tool to Investigate Metabolism and Treatment Response to Fingolimod in fEAE Rats

There is good evidence that with activation during inflammation, several immune cell subtypes undergo a metabolic switch away from oxidative metabolism towards anaerobic glycolytic metabolism[112–115]. Likewise, brain cells such as neurons and astrocytes, when under metabolic strain, can switch towards anaerobic ATP production, and both of these processes can lead to locally increased lactate production in areas of inflammation. These metabolic switches can be detected with hyperpolarised magnetic resonance techniques, and here I sought to understand the role of [1-^{13}C]ethylpyruvate MRS in probing metabolic changes and treatment response to fingolimod in the fEAE rat model of MS.

4.1 Metabolic Changes in Immune and Brain Cells in Inflammation

4.1.1 Immune Cell Metabolism

As explained in chapter 1, MS is a complex, immune-driven inflammatory disease which mobilises multiple components of the immune system against 'self' antigens. Mononuclear phagocytes (MNPs), including peripheral macrophages which migrate into the acute MS lesions in the CNS from the periphery, and microglia, the CNS's resident MNPs become activated and are key contributors to both the acute and chronic axonal damage seen in MS[1–3].

In their quiescent, pre-activated state, MNPs tend to undergo TCA cycle metabolism, producing ATP through oxidative phosphorylation[116]. However, when activated, MNPs have been shown to reprogram towards glycolytic metabolism in order to rapidly generate ATP, even in the presence of sufficient oxygen[116–118]. This metabolic switch is accompanied by an increase in lactate production,

and a concomitant reduction in bicarbonate production through reduced CO_2 generation in the link reaction. Guglielmetti *et al.* demonstrated, using hyperpolarised [1-^{13}C]pyruvate MRI in a toxin-induced cuprizone model of MS, that increased lactate production in the corpus callosum, was correlated with histological evidence of abundant activated microglia[79]. Repeats performed using knock-out mice with impaired microglial activation demonstrated significantly lower lactate production, emphasising both the importance of microglial activation in the pathophysiology of the cuprizone model of MS, and that activated microglial lactate is detectable using hyperpolarised [1-^{13}C] MRI[79].

Like MNPs in the innate immune system, quiescent T cells in the adaptive immune system utilise TCA cycle metabolism and may acquire TCA cycle substrates through a variety of pathways including glycolytic metabolism of glucose and ß-oxidation of fatty acids[112]. Effector T cells (T_{eff} cells) can be broadly split into subgroups by the CD4 and CD8 surface molecules they display. $CD4^+$ T cells become T helper (T_h) cells, which help modulate and coordinate immune responses, while $CD8^+$ T cells are cytotoxic. It has been shown that both naïve and memory T_{eff} cells switch towards anaerobic lactate production when activated[112,113,119]. The purpose of this switch has been suggested to be that glycolysis provides rapid ATP production, whilst also allowing T cells to adapt to the less oxygen-rich environments often encountered in acute inflammation[120]. Corroborating this theory, T cell receptor (TCR) engagement has been shown to induce expression of hypoxia-inducible factor (HIF) transcription factors, which upregulate transcription of the machinery needed for survival under hypoxic conditions, including that for glycolysis[45]. In an *in vitro* study using hyperpolarised ^{13}C MR, Can *et al.*[114] demonstrated that $CD4^+$ T cells, increase their lactate production when activated. Though regulatory T cells (T_{reg}) typically maintain TCA cycle metabolism, they too can generate lactate under certain conditions[121].

Taken together, these data indicate that the acute immune activation seen in MS lesions is likely to generate a net transition towards glycolytic metabolism and lactate production, and away from oxidative TCA cycle metabolism in inflammatory lesions.

4.1.2 Cerebral Metabolism

At rest, the brain avidly metabolises glucose[109]. Glucose traverses the BBB by uptake through glucose transporters (GLUTs) expressed on astrocytic end feet[115]. There is evidence, however, that neurons themselves may not always metabolise glucose directly. In fact, with compromised glucose supply, neurons are able to metabolise lactate as a respiratory substrate[109,122]. As mentioned in Chapter 1, glucose is metabolised via pyruvate to become lactate under aerobic stress, and the conversion of pyruvate to lactate is catalysed by the enzyme LDH. There are several isoforms of the LDH enzyme, with isoforms LDH1 and LDH5 being the most prominently expressed in the brain. LDH5 favours conversion of pyruvate to lactate, with the concomitant oxidation of nicotinamide adenine dinucleotide (NAD), and is present in astrocytes. Conversely, the LDH1 isoform favours the conversion of lactate to pyruvate and the production of reduced NAD (NADH) and is expressed in neurons themselves. Reaction outlines for the process of lactate production in astrocytes, and lactate utilisation in neurons are included in Fig. 16. Several authors have put forward the idea of a neuron-astrocyte lactate shuttle (illustrated in fig. 17), whereby astrocytes metabolise glucose via glycolysis, and produce lactate for use by other brain cells, including neurons. Astrocytic lactate production, which may be from glucose or monocarboxylates such as pyruvate taken up through GLUTs/MCTs on the endothelial end-foot membrane, or via glycogenolysis from astrocytic stored glycogen, is stimulated by neuronal activity. Extracellular glutamate released by neurons is taken up via a Na^+-dependent process, increasing Na^+/K^+ATPase activity and driving glycolytic ATP production, which is sustained after astrocytes' own metabolic needs have been met. Lactate is then released into the extracellular space, where it is taken up by neurons, and converted to pyruvate to be utilised as a respiratory substrate[109,115].

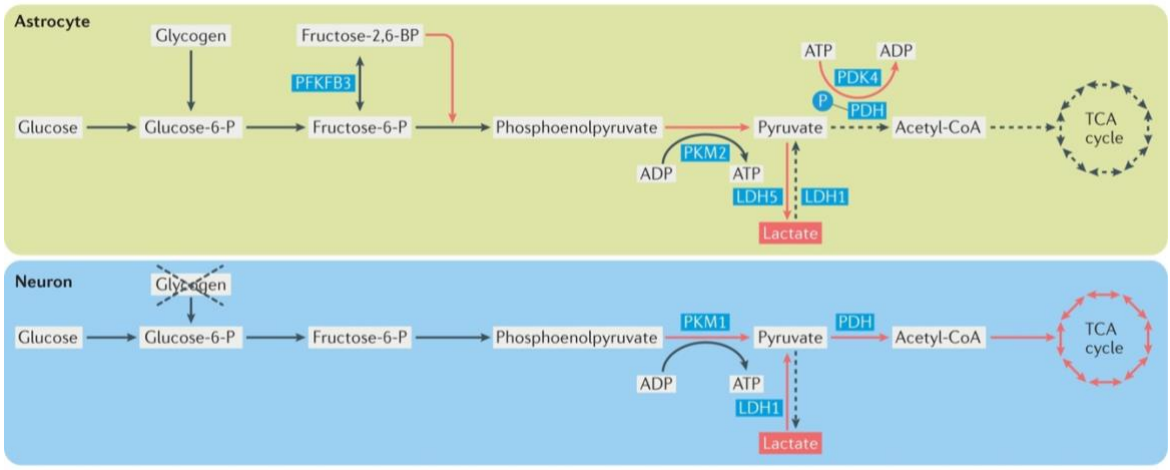


Figure 16. Reproduced from Magistretti and Allaman, 2018[123] Reaction schemes showing lactate production via LDH5 in astrocytes, and conversion of lactate to pyruvate through LDH1 in neurons. Red arrows indicate upregulated pathways, while dotted arrows indicate downregulated pathways. Astrocytic metabolism is characterised by glycogen and lactate production, in contrast to neurons, which do not produce glycogen, and utilise lactate as a respiratory substrate. PFK = phosphofructokinase, PFKFB3 = 6-phosphofructo-2-kinase/fructose-2,6-bisphosphatase, PKM1/2 = pyruvate kinase M1/2, LDH = lactate dehydrogenase, PDH = pyruvate dehydrogenase, PDK = pyruvate dehydrogenase kinase, TCA cycle = tricarboxylic acid cycle, ADP = adenosine diphosphate, ATP = adenosine triphosphate.

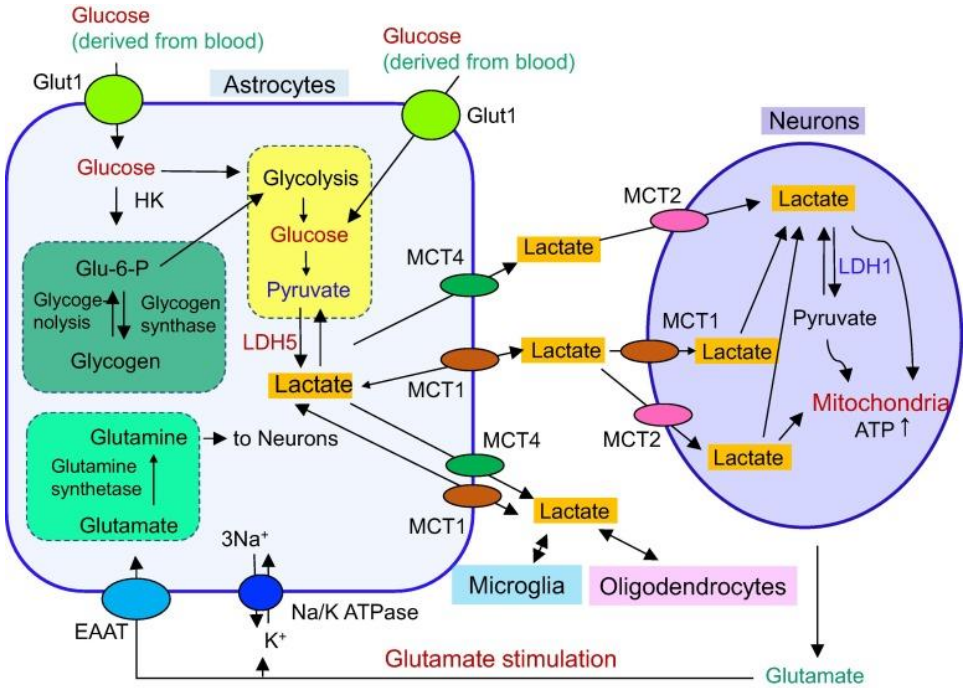


Figure 17. Reproduced from Yamagata, 2022[124] outlining the astrocyte-neuron lactate shuttle. Glucose taken up via astrocyte end feet is metabolised to pyruvate and lactate in response to increased Na^+/K^+ATPase activity triggered by increases in intracellular Na^+ secondary to glutamate uptake following synaptic activation. Lactate is shuttled out of astrocytes by MCTs 1 and 4, and taken up into neurons via MCT2, where lactate is converted to pyruvate via LDH1 for use as a respiratory substrate. Abbreviations: Glut1 = glucose transporter 1, HK = hexokinase, LDH = lactate dehydrogenase, MCT = monocarboxylate transporter, ATP = adenosine triphosphate, EAAT = excitatory amino acid transporter.

Therefore, with increased neuronal glutamate release during periods of neuronal activity, astrocytes are triggered to replenish and increase the extracellular pool of lactate available for neuronal metabolism.

With increased neuronal activity, cerebral energy demand rises from baseline. Repeated neuronal depolarisation and neurotransmitter release prompts increased Na^+/K^+ATPase activity to return membrane potential to resting potential, and neurotransmitter molecules must be taken up from synapses and stored for subsequent release. Task-induced increases in glucose uptake in humans have been noted to correlate with increased CBF, but only marginal increases in $CMRO_2$. This suggests that with increased local energy demand, glucose supply is increased by increasing perfusion, but that subsequent metabolism of glucose is not through oxidative phosphorylation, but instead through anaerobic metabolic pathways which are likely to generate lactate[109].

Together, these data suggest that under periods of strain, astrocytes will be stimulated to maintain a pool of extracellular lactate, which can be used by neurons as a respiratory substrate. As explained in Chapter 1, in the context of a demyelinating MS lesion, loss of the myelin sheath and sodium channel redistribution increase sodium leak across the axolemma, while mitochondrial and oxidative damage place the neuron under energetic strain. Neurons are unable to generate sufficient ATP to maintain normal resting potential, and consequently become hyper-excitable. The resultant neuronal glutamate release will drive astrocytic lactate production and excretion, which will be potentiated by glutamate release by activated MNPs.

In summary, both activated immune cells at sites of acute inflammation, and neurons and astrocytes from the brain itself are likely to increase lactate production at sites of acute inflammation such as that in MS lesions. This lactate production has been observed previously using proton MRS[125], however low signal-to-noise ratio (SNR) in proton MRS experiments limits the spatial and temporal resolution which can be achieved using this technique.

4.1.3 [1-^{13}C]Ethylpyruvate as a Tracer for Neuroinflammation

Hyperpolarised ^{13}C MRS represents an alternative to proton MRS, combining high SNR and rapid scan time with excellent biochemical resolution. Previous studies using hyperpolarised [1-^{13}C]pyruvate MRS have been successful in detecting acute inflammation outside the brain[126,127], and more recently, hyperpolarised [1-^{13}C]pyruvate MRS has been successfully used to image acute inflammation in the cuprizone mouse model of MS[79].

Here, I have used hyperpolarised [1-^{13}C]ethylpyruvate MRS to investigate metabolic changes in MS-like lesions in the fEAE rat model of MS with and without treatment with the S1PR modulator fingolimod. As explained in Chapter 1, [1-^{13}C]ethylpyruvate is a lipophilic analogue of [1-^{13}C]pyruvate, which allows direct diffusion of hyperpolarised ^{13}C-labelled tracer through the BBB in addition to uptake through MCTs, meaning a higher proportion of injected tracer reaches the brain parenchyma and enters metabolism within the short time window afforded by the T_1 of hyperpolarised [1-^{13}C]ethylpyruvate[24]. While detected [1-^{13}C]lactate signal may represent a combination intracellular, extracellular extravascular, and intravascular lactate, this signal is generated exclusively intracellularly, and thus represents the metabolic state of the tissue within the data collection area. While Guglielmetti *et al* have shown that hyperpolarised [1-^{13}C]pyruvate imaging is capable of detecting lesions in a toxic mouse model of MS[79], here I have chosen an immune-driven model, better mimicking the pathological process in MS. The fEAE model is uniquely suited for imaging studies due to a highly predictable lesion site, and the fact that the unaffected hemisphere can be used as a control. In addition, unlike the cuprizone model, the fEAE model does respond to treatment, and its response to fingolimod has been previously characterised[66].

4.2 Methods

4.2.1 Overview

Focal DTH lesions were prepared in 8 healthy Lewis rats by stereotactic injection of heat-treated BCG into the left striatum. 30 days were allowed for surgical wound healing, before lesion initiation by peripheral intradermal injection of BCG and complete Freund's adjuvant (CFA). Rats were randomly assigned to treatment and control groups, n=4 in each. The treatment group received a daily intraperitoneal injection of fingolimod for 7 days beginning on day 5 post-lesion initiation. Rats underwent [1-^{13}C]ethylpyruvate MRS on day 12 post-lesion initiation, and were culled for histology immediately afterwards.

4.2.2 Animal Handling and Anaesthesia

Experiments were conducted using 8 female Lewis rats. Animals were housed together in allergen-free bedding and had access to food and water *ad libitum*. Ethical approval was granted following review by both the University of Oxford Clinical Medicine Ethical Review Committee, and as part of the project license application. All animal experiments and procedures were performed out with the appropriate personal, project and institutional licences granted under the UK Animals (Scientific Procedures) Act 1986. All experiments were conducted in accordance with the University of Oxford Policy on the Use of Animals in Scientific Research. Anaesthesia was induced using 2.5% isoflurane with 60:40 O_2:N_2. Maintenance was with 2% isoflurane, and scanning took place with an inspired mixture of 60:40 O_2:N_2O. After final scanning, rats were killed by excess isoflurane inhalation, and death was confirmed by thoracotomy.

4.2.3 fEAE Lesion Generation and Treatment with Fingolimod

The process of DTH lesion generation is described elsewhere in greater detail[66,80,128]. In brief, rats were anaesthetised with 2% isoflurane and 100% O_2, and heat-treated BCG (10^5 cells in 1µL of 0.1M phosphate buffer solution) was injected stereotactically into the left striatum via a burr hole 1mm anterior and 3mm lateral to bregma at a depth of 4mm. 30 days were allowed for recovery and

healing of surgical wounds and cessation of local post-traumatic inflammation before lesion initiation. DTH lesion initiation was performed by intradermal injection of 0.75mg *Mycobacterium tuberculosis* in 50µL of complete Freund's adjuvant/saline emulsion into each hindlimb under anaesthesia.

Rats were randomly allocated to treated and untreated groups (n=4 per group). Rats allocated to the treatment group received an intraperitoneal injection of fingolimod 0.3 mg/kg/day in 0.5mL of saline once per day for 7 days starting on day 5 post-lesion initiation.

4.2.4 [1-^{13}C]Ethylpyruvate MRS and Analysis

All rats were imaged with hyperpolarised [1-^{13}C]ethylpyruvate MRS at day 12 post-lesion initiation. A [1-^{13}C]ethylpyruvate mixture containing AH111501 trityl radical and Dotarem gadolinium chelate was prepared as described in section 2.2.3. Hyperpolarised [1-^{13}C]ethylpyruvate underwent hyperpolarisation for 60-90 minutes at approximately 1K in a prototype 3.35T DNP system as described previously[16]. Dissolution was undertaken with pressurised, heated sodium hydroxide solution to achieve physiological temperature and pH. One millilitre of hyperpolarised [1-^{13}C]ethylpyruvate solution was injected over 4 seconds through a tail vein cannula, followed by a 300 µL saline flush.

Initial localiser images were acquired using a ^{1}H/^{13}C volume transmit/receive coil and a 3D gradient echo sequence (TR = 5ms, TE = 1ms**,** flip angle = 10°, RF spoiled, FOV = 60mm^{3}, acquisition matrix = 256 x 256 x 64, reconstruction matrix = 512 x 512 x 64). A 2D multi-echo B_0 mapping sequence was performed with subsequent automated shimming.

Hyperpolarised [1-^{13}C]ethylpyruvate spectroscopy was performed using a pulse-acquire sequence (excitation pulse = sinc, excitation pulse width 500µs, flip angle = 15º, TR = 0.5s, TE = 0.3ms slice thickness = 10 mm, slice gap = 1mm, number of slices = 2, temporal resolution = 1s, number of

time points = 240) using a single channel ^{13}C surface coil and $^{1}H/^{13}C$ quadrature volume transmit coil. Slices were placed over left and right cerebral hemispheres.

Spectra were summed in the frequency domain, phased, and fit in jMRUI using AMARES[129]. Ethylpyruvate, ethylpyruvate hydrate, pyruvate, pyruvate hydrate, and lactate were used as basis functions. Lactate:total carbon ratio was quantified and the mean for each hemisphere per rat calculated. Comparisons were made between ipsilateral and contralateral hemispheres, and between treated and untreated groups.

4.2.5 Proton MRI

After [1-^{13}C]ethylpyruvate MRS, rats were transferred whilst anaesthetised to a dedicated neuro-imaging cradle with a 4-channel ^{1}H array placed over the brain with bite bar and ear pins for consistent positioning. As described in section 3.2.4, a 3D gradient echo sequence was performed and B_0 shimming applied. A bolus of 200µL of Dotarem gadolinium chelate contrast agent was administered via tail vein catheter. 5 minutes after injection, a 3D gradient echo sequence (TR = 5ms, TE = 1ms**,** flip angle = 12°, RF spoiled, FOV = 40mm^3, acquisition matrix = 256 x 256 x 64, reconstruction matrix = 512 x 512 x 64) was acquired.

4.2.6 Histology

The procedure used for tissue fixation and staining has been previously described[66]. Briefly, after death each rat was perfused with heparinised saline and 200mL of 2% periodate lysine paraformaldehyde. Brain tissue was collected, further fixed in periodate lysine paraformaldehyde, stored in 30% sucrose solution, and cooled to 4ºC. Brain tissue was then frozen in liquid nitrogen. 10µm brain sections were cut and stained with cresyl violet before photography.

4.2.7 Statistical Analysis

All data was assumed to be non-normally distributed. Lactate:total carbon ratio was compared between ipsilateral and contralateral hemispheres relative to lesion position in both treated and untreated groups. Ipsilateral and contralateral lactate:total carbon ratio was also compared between treated and untreated groups. All comparisons were made by Mann-Whitney test. Statistics were conducted in R.

4.3 Results

4.3.1 Hyperpolarised [1-^{13}C]Ethylpyruvate MRS

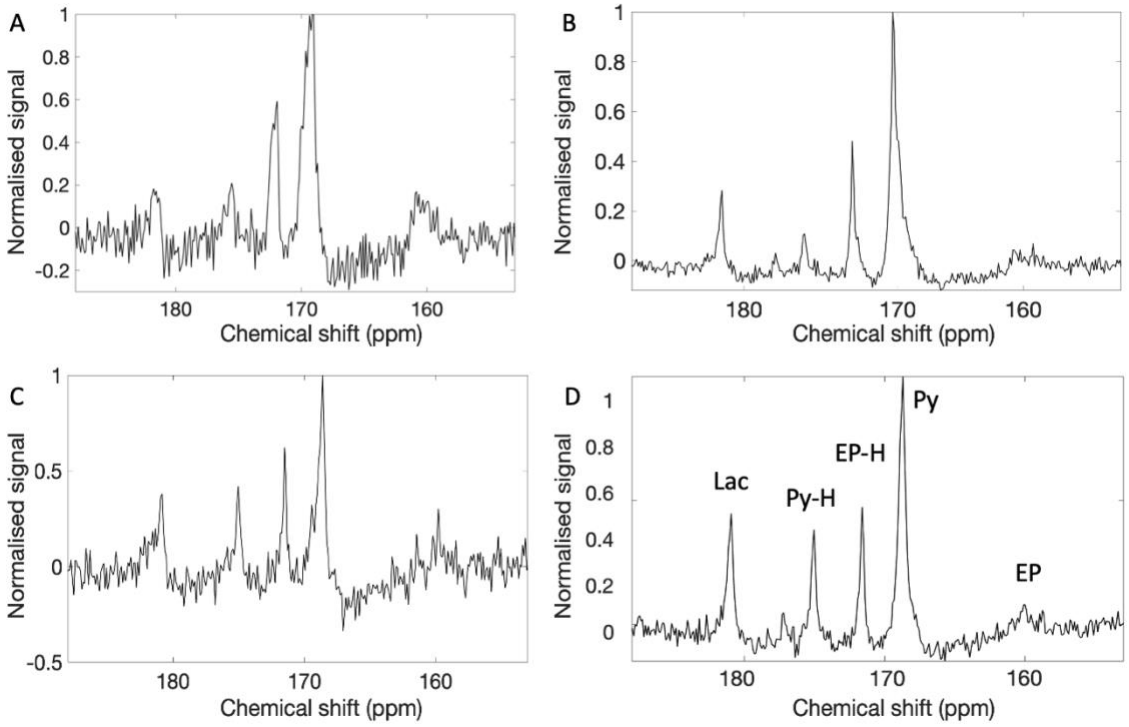


Figure 18. Representative summed spectra from hyperpolarised [1-^{13}C]ethylpyruvate spectroscopy from the contralateral (A) and ipsilateral (B) untreated and the ipsilateral (C) and contralateral (D) fingolimod-treated rodent brain at day 12 post-lesion initiation. Spectral peaks identified in (D) as lactate (Lac), pyruvate hydrate (Py-H), ethylpyruvate hydrate (EP-H), pyruvate (Py), and ethylpyruvate (EP). No line broadening is applied.

Hyperpolarised ^{13}C MRS was used to probe cerebral metabolism in the hemispheres ipsilateral and contralateral to the fEAE lesion in treated (n=4) and untreated (n=4) rats, and example summed spectra are shown in Fig. 18. Data is summarised in Fig. 19. Comparison of the contralateral and ipsilateral lactate:total carbon ratios within the treated and untreated groups revealed a higher

lactate:total carbon ratio in the ipsilateral hemisphere of untreated rats (p=0.02), however no difference was seen between hemispheres in the treated rat group (p=0.91). There was no difference in ipsilateral (p=0.49) or contralateral (p=0.11) hemispheric lactate:total carbon ratio between the treated and untreated groups.

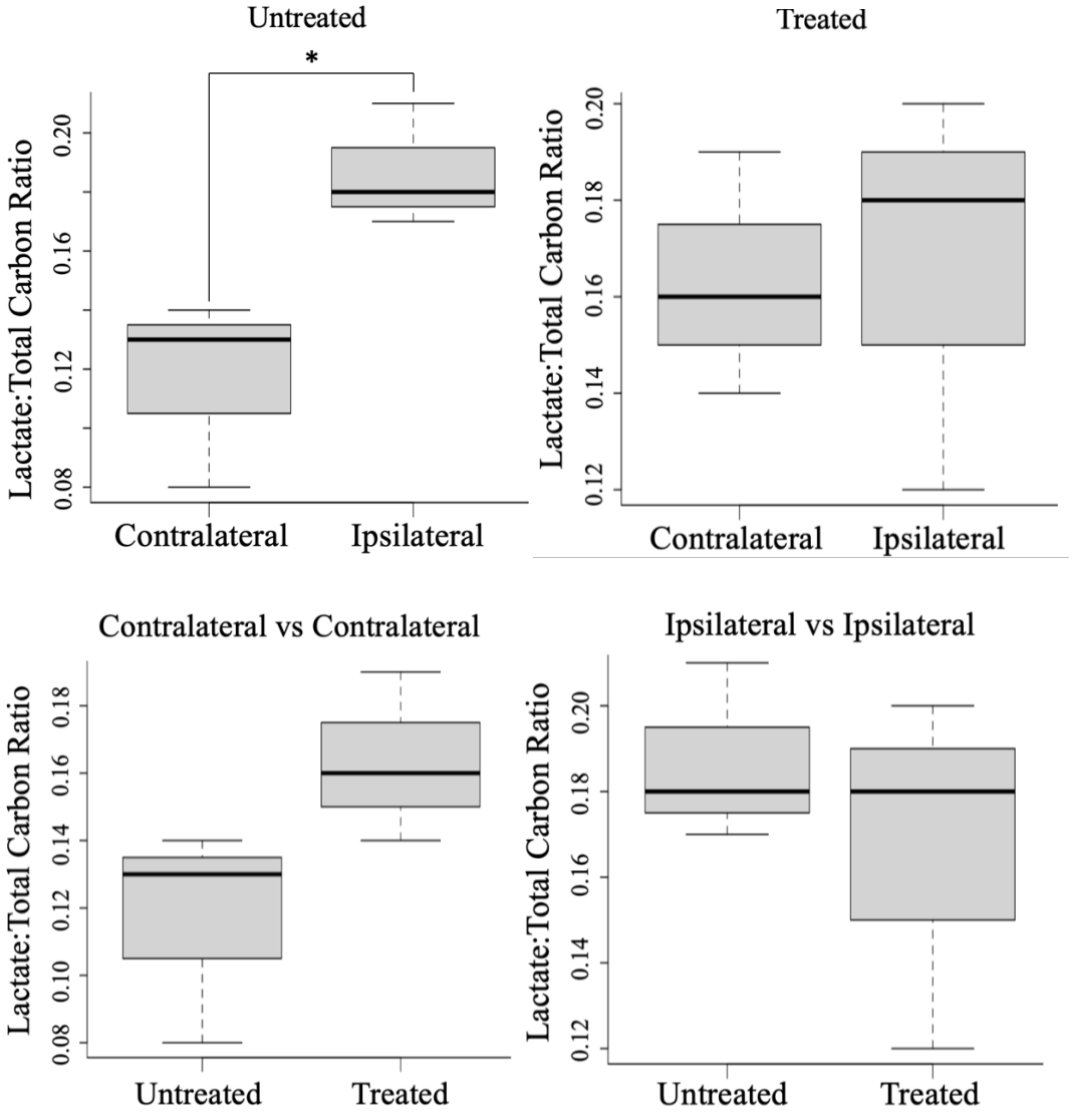


Figure 19. Lactate signal is raised in the ipsilateral hemisphere of untreated fEAE rats. Summary of hyperpolarised [1-^{13}C]ethylpyruvate MRS data comparing ipsilateral and contralateral hemispheric lactate:total carbon ratios between hemispheres, and between treated and untreated fEAE rats. n=4 in treated and untreated groups. *p<0.05.

4.3.2 Proton MRI

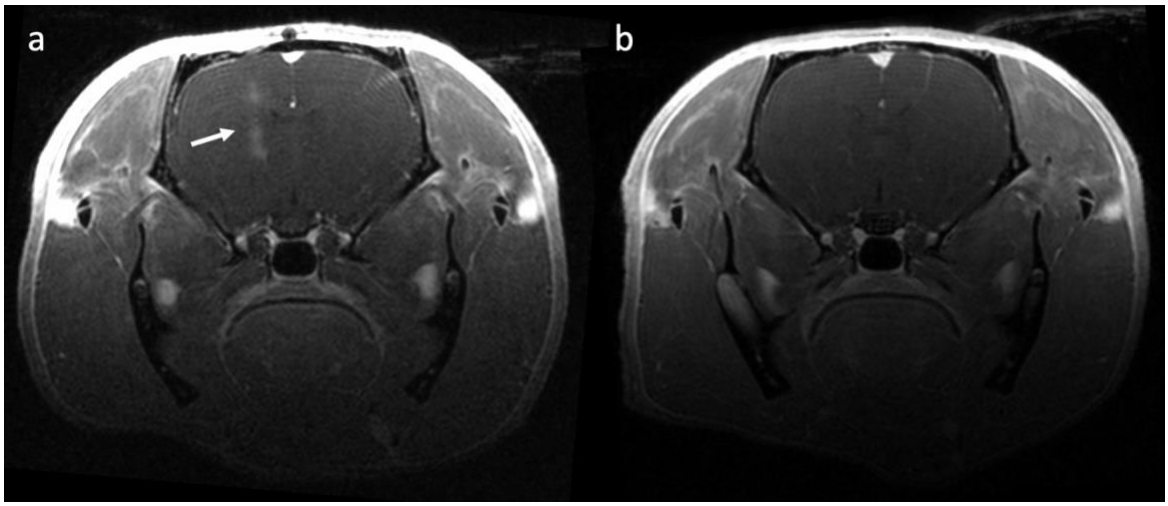


Figure 20. Representative gadolinium-enhanced MRI images showing axial sections through the brain in rats from both the untreated (a) and treated (b) groups. An area of gadolinium enhancement can be seen to the left of the midline in the untreated rat, indicating an area of BBB breakdown, which is not present in the corresponding area in the treated rat, and is indicated by a white arrow.

Gadolinium-enhanced proton MRI was attempted for each rat after ^{13}C spectroscopy. Due to tail vein blockage or movement, imaging was successful in 2 treated, and 3 untreated rats. As illustrated in Fig. 20a, gadolinium enhancement was visible in the untreated group to the left of the midline, in an area corresponding to the approximate location of the stereotactic injection site. No gadolinium enhancement was visible in any of the rats that received fingolimod treatment (Fig. 20b).

4.3.3 Histology

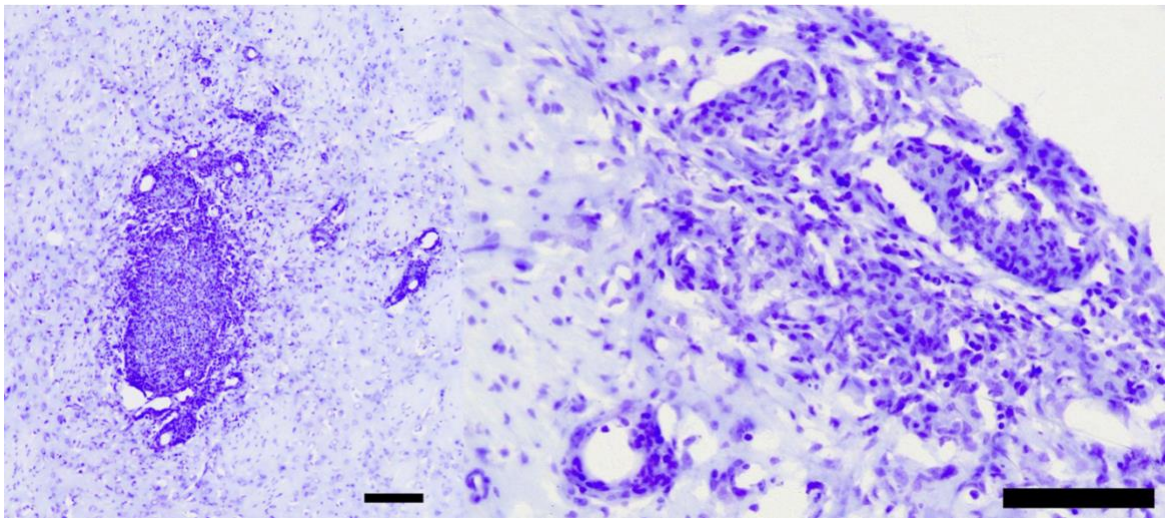


Figure 21. Representative cresyl violet-stained histological images of DTH lesions from two rats from the untreated group. Scale markers indicate 100 µm.

Cresyl violet staining revealed clusters of cells in the left striatum consistent with a DTH lesion in two of four untreated rats (Fig. 21). Histological fixation was unsuccessful in the remaining untreated rats. No lesion was visualised on examination of sections from treated rats.

4.4 Discussion

As laid out in section 4.1, immune cell activation and cerebral energy dysregulation at sites of acute inflammation cause a local metabolic shift towards lactate production. This project aimed to validate hyperpolarised [1-^{13}C]ethylpyruvate as a metabolic tracer to detect this shift, and as a method of detecting treatment response to fingolimod in the fEAE model of MS.

4.4.1 Confirmation of Lesion Development

Key to making assertions about metabolic changes secondary to the presence of a DTH lesion in the left striatum, is to demonstrate successful lesion generation. Here this was planned to be achieved in two ways: confirmation of lesion position on Gd-enhanced MRI, and direct observation of immune cell accumulation through immunohistochemistry.

In the treated group, we experienced Gd injection failure in two of four rats, and similarly in one of four untreated rats. As demonstrated in Fig. 20a, Gd enhancement was seen in the left hemisphere of the untreated rats in a location corresponding to the location of stereotactic injection. This suggests that there was BBB breakdown in this region and is therefore suggestive of successful lesion generation. In the treated rats, no Gd enhancement was seen. Given the problems with tail vein catheter patency experienced throughout our experiments, it is possible that an inadequate Gd shot was delivered in these rats. However, more likely is that fingolimod treatment prevented lesion development, or facilitated BBB re-sealing before scanning on day 12, masking the presence of any lesion.

Histological analysis of brain tissue was planned to include immunohistochemical staining for glial fibrillary acidic protein (G-FAP), ionised calcium-binding adaptor molecule 1 (IBA-1), and CD3, which would highlight activated astrocytes, activated microglia, and lymphocytes respectively. The initial process of loading brain slices onto slides for staining was unsuccessful, possibly due to a fault in the slides used. As a result, slices did not adhere properly to the slide surface, and no immunohistochemical analysis was successfully achieved. The cresyl violet counterstain was successfully applied in a minority of cases, and therefore basic visualisation of tissue architecture was possible. No areas suggestive of lesion development were identified in the treated rat group. However, in both treated rats in which the cresyl violet stain was successfully applied, clusters of cells consistent with lesion development (Fig. 21) were visualised in the left striatum, suggesting the presence of a DTH lesion.

Taken together, these data suggest that lesions were successfully generated in the untreated group. Gadolinium-enhanced MRI and histological analysis demonstrate the presence of BBB breakdown and cell clustering at the site where a lesion would be expected. However, immunohistochemical confirmation of appropriate immune cell clustering at the lesion site would provide final confirmation that DTH lesions are truly present.

Surprisingly, no gadolinium enhancement or changes in tissue architecture were seen at the injection site in the treated rats. Anthony *et al.*[66] found a 52% reduction in BBB breakdown in rats treated with 0.3mg/kg/day oral fingolimod on days 5-12 after lesion activation compared to untreated rats, and a significant reduction in the recruitment of both lymphocytes and activated microglia. Lesions were, however, detectable with both Gd-enhanced MRI and immunohistochemistry. One difference in protocol between these experiments and our own is the method of fingolimod administration. While the dose of fingolimod administered is the same in both protocols, Anthony *et al.* administered fingolimod by oral gavage, whereas here administration was by intraperitoneal injection. The oral bioavailability of fingolimod is around 90% in humans[130], however it is possible that some fingolimod may not be ingested during the process of oral gavage, and that further

intraperitoneal injection may provide higher bioavailability, which may have resulted in a more pronounced effect of fingolimod in preventing lesion development. Another possibility is that sub-optimal Gd injections in the treated rats resulted in insufficient injected gadolinium to highlight the less-extensive BBB breakdown in the treated group. Further, it is possible that had immunohistochemistry been successful, it may have highlighted a lesion area with a high concentration of activated immune cells which was not apparent on inspection of tissue architecture alone.

4.4.2 Lesion Detection and Treatment Response with [1-^{13}C]Ethylpyruvate MRS

Lactate:total carbon ratios from summed spectra from hemispheres ipsilateral and contralateral to induced striatal DTH lesions were compared to each other and between treated and untreated groups. Comparison of the ipsilateral and contralateral hemispheres in untreated rats revealed a higher lactate:total carbon ratio in the hemisphere ipsilateral to the DTH lesion. This difference was obliterated in treated rats. This difference is likely driven by the prevention of lymphocyte migration from secondary lymphoid tissue into the fEAE lesion. Not only does this reduce the abundance of lactate-producing activated immune cells in the lesion, it also reduces downstream effects resulting from cytokine release and innate immune cell recruitment which follow from activated lymphocyte recruitment. It is also possible that the metabolic differences presented here are affected by differential blood flow to lesion and non-lesion hemispheres. Interpretation of metabolic data are predicated on the assumption that ethylpyruvate transport into the CNS through MCTs, and lactate production through LDH are saturated, but that de-esterification of ethylpyruvate by esterases is unsaturated. If the conversion of ethylpyruvate to pyruvate were to become rate-limiting, perhaps due to off-target effects of the fingolimod treatment agent, it would result in undersaturation of LDH or PDH, and the extent of undersaturation would be unknown. Upon analysis of the resultant metabolite ratios, it would be unclear if the ratio was a true reflection of the balance of bicarbonate and lactate within the cell, or simply a result of substrate shortage to one or both enzymes. Similarly, if one hemisphere were to be under-perfused to the extent that MCTs and LDH are not saturated,

then the metabolite ratios detected will become a function of perfusion to that hemisphere, and the metabolite ratios obtained would not reflect the metabolic state of the cell, but rather local perfusion. Paired perfusion MR measurements were attempted in order to unpick this, however due to technical failures these data were not successfully obtained. Perhaps surprisingly, no difference in lactate:total carbon ratio was observed between ipsilateral hemispheres in treated and untreated rats, but a trend towards higher lactate production was observed in the treated contralateral hemisphere. S1PRs are present throughout the body, and are expressed in every cell in the CNS. Aside from its effects on immune cell trafficking, to which much of its efficacy in MS is attributed, fingolimod has a plethora of other CNS effects. BBB permeability, astrocytic gap junctional signalling, calcium handling and NO signalling, microglial cytokine and neurotrophin production, neuronal glutamate release, and oligodendrocyte apoptosis are all affected by S1P signalling[131]. It is possible that this web of off-target effects if responsible for the contralateral hemispheric metabolic differences found here.

These data suggest that though treatment response to fingolimod was not detectable by comparison of ipsilateral hemispheres between treated and untreated groups, hyperpolarised [1-^{13}C]ethylpyruvate MRS has the biochemical sensitivity to detect inflammatory changes in lactate ratio between ipsilateral and contralateral hemispheres in untreated rats. Further, assuming that lesions were generated and suppressed by fingolimod administration, the lack of a difference in lactate:total carbon ratio between ipsilateral and contralateral hemispheres in treated rats suggests that this technique also has the biochemical sensitivity to detect treatment response. To confidently make this assertion, however, further experiments must be done in which lesion generation in treated rats is corroborated by MRI or histology.

4.4.3 Conclusions

These results represent a promising step in establishing hyperpolarised [1-^{13}C]ethylpyruvate as a useful metabolic tracer for translation into humans. To the author's knowledge, this represents the first use of [1-^{13}C]ethylpyruvate rather than [1-^{13}C]pyruvate in examining neurological disease. This builds on work put forward by Hurd *et al.*[24] who suggested that [1-^{13}C]ethylpyruvate may be more

suitable than [1-^{13}C]pyruvate for neuroimaging due to its lipophilicity, and demonstrated that hyperpolarised [1-^{13}C]ethylpyruvate could be used for neuroimaging in healthy animals. Secondly, this work differs from that of Guglielmetti *et al.*[79], who used hyperpolarised [1-^{13}C]pyruvate MRI to interrogate the toxin-induced cuprizone mouse model of MS. Here, I have employed an immune-driven rather than a toxin-driven model of MS and have included a treatment arm. Therefore, these data are the first evidence that hyperpolarised ^{13}C MRI/MRS is sensitive in lesion detection in an immune-driven model of MS, and that this technique may be able to detect treatment response in this MS model.

With preliminary studies in healthy patients already conducted using hyperpolarised [1-^{13}C]pyruvate[111] MR, the possibility of translating this technique into clinical practice seems realistic. Though preclinical work is still at an early stage, it seems that hyperpolarised ^{13}C MR has the potential to both detect active lesions, and track changes in lesion activity with treatment. The niche this technique could fill in MS management may be in the monitoring of patients with known disease, rather than in initial diagnosis. Serial hyperpolarised ^{13}C MRI may be able to track lesion activity by using bicarbonate:lactate or lactate:total carbon ratio as a proxy for local disease activity. This has the potential to prove more sensitive to changes in response to treatment than current imaging monitoring methods and may facilitate rapid drug switching. Patients may be scanned three or six months after beginning a certain treatment course and switched to another if hyperpolarised ^{13}C MR-measured lesion activity has not reduced. Likewise, if a rapid and reliable measure of lesion activity could be developed, it would aid drug development as well as patient monitoring.

Before these clinical applications have a chance to come to fruition, several further preclinical studies are needed. This study used hyperpolarised ^{13}C MRS to examine differences between affected and unaffected hemispheres, however while spectroscopy may prove to be useful in assessment of diffuse disease, hyperpolarised ^{13}C MRI is more likely to be useful in everyday clinical settings for the detection and monitoring of specific lesions. Preclinical studies similar to this one using hyperpolarised ^{13}C MRI would assess whether this technique is sensitive enough to

pick out individual lesions, and the addition of perfusion MR to the experimental protocol would provide valuable information about relative rates of tracer delivery to lesion and non-lesion brain areas. Likewise, successful Gd-enhanced MRI and immunohistochemical confirmation of lesion generation would allow observed metabolic changes to be confidently attributed to DTH lesions. A longitudinal study in which fEAE rats were imaged serially at several time points including a pre-lesion initiation baseline timepoint would be useful in validating the technique in terms of its ability to monitor disease process over time. Sham injection control rats in which saline is injected into the striatum rather than heat-treated BCG would definitively unpick post-surgical inflammation from inflammation generated by lesion activation. Given enough resource, it would be interesting to design a study which compared serial hyperpolarised ^{13}C MRI in untreated fEAE rats and in several different MS treatments in addition to fingolimod, for example the anti-CD20 monoclonal antibody ocrelizumab.

Chapter 5 – Closing Comments

In this final chapter, I have included some of my reflections on the last year, and the process of completing my master's degree under unusual circumstances.

The COVID-19 pandemic has reshaped my experience of this year completely and has also forced me to adapt in my research as well. Access to the lab was very limited during the first half of my degree, and apart from having to adapt my experimental design to accommodate this, I have done much of my learning from the isolation of my own home. Increased autonomy in your learning is part of moving from undergraduate to postgraduate level, and while I have enjoyed the freedom to read around my subject, I certainly missed the camaraderie and the ease with which one can ask questions that comes with a usual in-person lab environment. In exchange, I feel that I have improved my skills in self-directed learning, self-motivation, and time management, and these will serve me well in my future career.

As mentioned above, my experimental lab time was cut down significantly by the COVID-19 pandemic. My initial research proposal included several scanning time points, a larger cohort of rats with a sham injection group, and larger n numbers in each group. However, with reduced time it is important to adapt investigative strategy. Alongside restricted lab time, and competition for magnet booking once the department reopened, supplies of certain necessary chemicals and of the experimental animals themselves were difficult to access. These challenges forced us to drill down to the essentials of the study I wanted to conduct and vindicated the choice of experimental model. Despite limited access to animals and lab time, the fEAE model allows the use of the unaffected hemisphere as a control, and therefore allowed us to adapt the study to include simply treatment and non-treatment groups, with each rat acting as its own paired control. The number of scanning time points was also reduced, and was planned to include simply a baseline pre-lesion-initiation hyperpolarised [1-^{13}C]ethylpyruvate MRI scan, proton MRI, and a repeat at 12 days after lesion initiation, with rats culled for histology.

Unfortunately, several equipment failures further held back experimental dates. A pump failure on the DNP hyperpolariser prevented hyperpolarised ^{13}C experimental work for several weeks, and the fault recurred during our baseline experimental data collection, meaning that I did not obtain any usable hyperpolarised ^{13}C MRI data from our baseline time point. As our lesions were induced immediately after scanning, I was unable to delay the experiments for a second attempt to collect baseline data. At day 12 after lesion-induction, due to an unexpected failure of the 2-channel volume coil used for hyperpolarised ^{13}C MRI, instead a surface coil was used to gather hyperpolarised ^{13}C MRS data. While we successfully gathered hyperpolarised ^{13}C MRS data at this 12-day time point, problems with blocked or tissued rat tail veins meant that we were only able to gather proton perfusion and gadolinium-enhanced MRI data on five of eight rats, and only two within the treated experimental group. These data would have provided corroboration of lesion size and position and added interesting information regarding perfusion changes in acute MS lesions. Unfortunately, as no statistical analysis could be performed on an n of 2 in the treated group, and data from the untreated group did not provide any statistically significant results or give evidence which could support or refute the points made in this thesis, these perfusion MRI data were not presented. In future studies, however, perfusion MRI would be a useful adjunct to hyperpolarised ^{13}C MRI. Lastly, unsuccessful immunohistochemical analysis of tissue samples rendered the interpretation of metabolic data more difficult, and more limited. In future projects, I would hope to be able to link changes in lesion activity and treatment response to metabolic data through histological analysis.

One problem with the current protocol is that both hyperpolarised ^{13}C MRI and proton perfusion MRI require a tail vein injection. Hyperpolarised ^{13}C MRI is performed first, and often follows immediately after tail vein cannula insertion. However, after hyperpolarised ^{13}C MRI, rats are removed from the scanner, and transferred to a separate cradle, before being reinserted into the magnet an receiving their gadolinium injection. It is possible that the process of moving between magnet and cradles often causes the tail vein cannula to shift, potentially compromising the subsequent gadolinium bolus. Further, the longer a tail vein cannula is *in situ* the higher the chance

of clotting in the line, which may also prevent bolus flushing. There is a neuro-coil currently on the market which would facilitate both ^{13}C and proton scanning in the same cradle, which may prevent the tail vein cannula from becoming shifted between scanning types. As the fEAE model takes at least 30 days to prepare, and having started later than anticipated, repeat experiments were not possible, which led us to the experimental design presented above.

While the challenges outlined above resulted in a substantially different project to the one I planned when enrolling, I feel that it has given me an excellent introduction to research and the practicalities of the research process. I have developed my independent learning and research skills, teaching myself the basics of coding in MATLAB and the physics of MRI, both of which I plan to put to use in the future as a radiologist, as well as reviewing a large amount of literature in the writing of this thesis. I have realised the importance of adaptability and resourcefulness in modifying research plans in response to unexpected events and feel that I have a greater insight into the role of the researcher, which will stand me in good stead when applying for a radiology academic clinical fellowship, and hopefully a PhD in the future.

On a personal note, this year has been challenging from more than an academic standpoint. Unable to see friends and loved ones for much of the year, this year has been difficult for many people. After catching COVID-19 myself in January while working in A&E, I was unable to study for several weeks, and worked hard to catch up on the time that I had missed. Nevertheless, I am proud of the project I have managed to produce, and although some things did not go to plan, I have developed a lot both academically and personally.

Bibliography

1. Compston, A. & Coles, A. Multiple sclerosis. *The Lancet* vol. 372 1502–1517 (2008).
2. Thompson, A. J., Baranzini, S. E., Geurts, J., Hemmer, B. & Ciccarelli, O. Multiple sclerosis. *The Lancet* vol. 391 1622–1636 (2018).
3. Lassmann, H. Multiple Sclerosis Pathology. *Cold Spring Harb. Perspect. Med.* **8**, (2018).
4. Hauser, S. & Cree, B. Treatment of Multiple Sclerosis: A Review. *Am. J. Med.* **133**, 1380-1390.e2 (2020).
5. Thompson, A. J. *et al.* Diagnosis of multiple sclerosis: 2017 revisions of the McDonald criteria. *The Lancet Neurology* vol. 17 162–173 (2018).
6. Plewes, D. B. & Kucharczyk, W. Physics of MRI: A primer. *Journal of Magnetic Resonance Imaging* vol. 35 1038–1054 (2012).
7. Currie, S., Hoggard, N., Craven, I. J., Hadjivassiliou, M. & Wilkinson, I. D. Understanding MRI: Basic MR physics for physicians. *Postgraduate Medical Journal* vol. 89 209–223 (2013).
8. Gadian, D. G. *NMR and its applications to living systems*. (Oxford University Press, 1995).
9. Socha, O. & Dračínský, M. Dimerization of Acetic Acid in the Gas Phase-NMR Experiments and Quantum-Chemical Calculations. *Molecules* **25**, (2020).
10. Faghihi, R. *et al.* Magnetic Resonance Spectroscopy and its Clinical Applications: A Review. *Journal of Medical Imaging and Radiation Sciences* vol. 48 233–253 (2017).
11. Shah, N. J., Worthoff, W. A. & Langen, K. J. Imaging of sodium in the brain: A brief review. *NMR in Biomedicine* vol. 29 162–174 (2016).
12. Leach, M. *et al.* Measurements of human breast cancer using magnetic resonance spectroscopy: a review of clinical measurements and a report of localized 31P measurements of response to treatment. *NMR Biomed.* **11**, 314–340 (1998).
13. Schroeder, M., Clarke, K. & Tyler, D. Hyperpolarized magnetic resonance: a novel technique for the in vivo assessment of cardiovascular disease. *Circulation* **124**, 1580–1594 (2011).
14. Lewis, A. J. M., Tyler, D. J. & Rider, O. Clinical Cardiovascular Applications of Hyperpolarized Magnetic Resonance. *Cardiovasc. Drugs Ther.* **34**, 231–240 (2020).
15. Harris, T. *et al.* The Effect of Gadolinium Doping in [13C6, 2H7]Glucose Formulations on 13C Dynamic Nuclear Polarization at 3.35 T. *Chemphyschem* **21**, 251–256 (2020).
16. Ardenkjær-Larsen, J. H. *et al.* Increase in signal-to-noise ratio of >10,000 times in liquid-state NMR. *Proc. Natl. Acad. Sci.* **100**, 10158–10163 (2003).
17. Nelson, S. J. *et al.* Metabolic imaging of patients with prostate cancer using hyperpolarized [1-13C]pyruvate. *Science Translational Medicine* vol. 5 (2013).
18. Halestrap, A. & Wilson, M. The monocarboxylate transporter family--role and regulation. *IUBMB Life* **64**, 109–119 (2012).
19. Schwartz, L., Supuran, C. & Alfarouk, K. The Warburg Effect and the Hallmarks of Cancer. *Anticancer. Agents Med. Chem.* **17**, 164–170 (2017).
20. Obermeier, B., Verma, A. & Ransohoff, R. The blood-brain barrier. *Handb. Clin. Neurol.* **133**, 39–59 (2016).
21. Miller, J. J. *et al.* 13C Pyruvate Transport Across the Blood-Brain Barrier in Preclinical Hyperpolarised MRI. *Sci. Rep.* **8**, (2018).
22. Fink, M. Ethyl pyruvate: a novel anti-inflammatory agent. *J. Intern. Med.* **261**, 349–362 (2007).
23. Grist, J. T. *et al.* Hyperpolarized 13C MRI: A novel approach for probing cerebral metabolism in health and neurological disease. *Journal of Cerebral Blood Flow and Metabolism* (2020) doi:10.1177/0271678X20909045.
24. Hurd, R. E. *et al.* Metabolic imaging in the anesthetized rat brain using hyperpolarized [1-13C] pyruvate and [1-13C] ethyl pyruvate. *Magn. Reson. Med.* **63**, 1137–1143 (2010).
25. Browne, P. *et al.* Atlas of multiple sclerosis 2013: A growing global problem with widespread inequity. *Neurology* vol. 83 1022–1024 (2014).

26. Kobelt, G., Thompson, A., Berg, J., Gannedahl, M. & Eriksson, J. New insights into the burden and costs of multiple sclerosis in Europe. *Mult. Scler.* **23**, 1123–1136 (2017).
27. Thompson, A. J. *et al. Primary progressive multiple sclerosis*. *Brain* vol. 120 (1997).
28. Polman, C. *et al.* Diagnostic criteria for multiple sclerosis: 2010 revisions to the McDonald criteria. *Ann. Neurol.* **69**, 292–302 (2011).
29. Sorensen, P. *et al.* The apparently milder course of multiple sclerosis: changes in the diagnostic criteria, therapy and natural history. *Brain* **143**, 2637–2652 (2020).
30. Confavreux, C. & Vukusic, S. The clinical course of multiple sclerosis. *Handb. Clin. Neurol.* **122**, 343–369 (2014).
31. Hemmer, B., Kerschensteiner, M. & Korn, T. Role of the innate and adaptive immune responses in the course of multiple sclerosis. *The Lancet Neurology* vol. 14 406–419 (2015).
32. Witte, M. E., Mahad, D. J., Lassmann, H. & van Horssen, J. Mitochondrial dysfunction contributes to neurodegeneration in multiple sclerosis. *Trends in Molecular Medicine* vol. 20 179–187 (2014).
33. Stinissen, P., Medaer, R. & Raus, J. *Myelin reactive T cells in the autoimmune pathogenesis of multiple sclerosis*. *Multiple Sclerosis* vol. 4 http://www.stockton-press.co.uk/ms (1998).
34. Procaccini, C., De Rosa, V., Pucino, V., Formisano, L. & Matarese, G. Animal models of Multiple Sclerosis. *Eur. J. Pharmacol.* **759**, 182–191 (2015).
35. Sawcer, S., Franklin, R. & Ban, M. Multiple sclerosis genetics. *Lancet. Neurol.* **13**, 700–709 (2014).
36. Spencer, J., Bell, J. & DeLuca, G. Vascular pathology in multiple sclerosis: reframing pathogenesis around the blood-brain barrier. *J. Neurol. Neurosurg. Psychiatry* **89**, 42–52 (2018).
37. Stys, P., Zamponi, G., van Minnen, J. & Geurts, J. Will the real multiple sclerosis please stand up? *Nat. Rev. Neurosci.* **13**, 507–514 (2012).
38. Kleine, T. & Benes, L. Immune surveillance of the human central nervous system (CNS): different migration pathways of immune cells through the blood-brain barrier and blood-cerebrospinal fluid barrier in healthy persons. *Cytometry. A* **69**, 147–151 (2006).
39. Kermode, A. *et al.* Breakdown of the blood-brain barrier precedes symptoms and other MRI signs of new lesions in multiple sclerosis. Pathogenetic and clinical implications. *Brain* **113 (Pt 5**, 1477–1489 (1990).
40. Davalos, D. *et al.* Fibrinogen-induced perivascular microglial clustering is required for the development of axonal damage in neuroinflammation. *Nat. Commun.* **3**, (2012).
41. Montalban, X. *et al.* Ocrelizumab versus Placebo in Primary Progressive Multiple Sclerosis. *N. Engl. J. Med.* **376**, 30–31 (2017).
42. Cohen, J. *et al.* Oral fingolimod or intramuscular interferon for relapsing multiple sclerosis. *N. Engl. J. Med.* **362**, 402–415 (2010).
43. Polman, C. *et al.* A randomized, placebo-controlled trial of natalizumab for relapsing multiple sclerosis. *N. Engl. J. Med.* **354**, 899–910 (2006).
44. de Barcelos, I. P., Troxell, R. M. & Graves, J. S. Mitochondrial dysfunction and multiple sclerosis. *Biology (Basel).* **8**, (2019).
45. Galgani, M., De Rosa, V., La Cava, A. & Matarese, G. Role of Metabolism in the Immunobiology of Regulatory T Cells. *J. Immunol.* **197**, 2567–2575 (2016).
46. Agrawal, S. *et al.* Dystroglycan is selectively cleaved at the parenchymal basement membrane at sites of leukocyte extravasation in experimental autoimmune encephalomyelitis. *J. Exp. Med.* **203**, 1007–1016 (2006).
47. Lu, F. *et al. Oxidative damage to mitochondrial DNA and activity of mitochondrial enzymes in chronic active lesions of multiple sclerosis a b c a a d*. *Journal of the Neurological Sciences* vol. 177 www.elsevier.com/locate/jns (2000).
48. Su, K., Bourdette, D. & Forte, M. Mitochondrial dysfunction and neurodegeneration in multiple sclerosis. *Frontiers in Physiology* vol. 4 JUL (2013).
49. Mahad, D., Lassmann, H. & Turnbull, D. Review: Mitochondria and disease progression in multiple sclerosis. *Neuropathology and Applied Neurobiology* vol. 34 577–589 (2008).

50. Irvine, K. & Blakemore, W. Remyelination protects axons from demyelination-associated axon degeneration. *Brain* **131**, 1464–1477 (2008).
51. Trapp, B. D. & Stys, P. K. Virtual hypoxia and chronic necrosis of demyelinated axons in multiple sclerosis. *The Lancet Neurology* vol. 8 280–291 (2009).
52. Lassmann, H. Hypoxia-like tissue injury as a component of multiple sclerosis lesions. *J. Neurol. Sci.* **206**, 187–191 (2003).
53. Ciccarelli, O. *et al.* Pathogenesis of multiple sclerosis: Insights from molecular and metabolic imaging. *The Lancet Neurology* vol. 13 807–822 (2014).
54. Amorini, A. M. *et al.* Serum lactate as a novel potential biomarker in multiple sclerosis. *Biochim. Biophys. Acta - Mol. Basis Dis.* **1842**, 1137–1143 (2014).
55. Cotton, F., Weiner, H., Jolesz, F. & Guttman, C. MRI contrast uptake in new lesions in relapsing-remitting MS followed at weekly intervals. *Neurology* **60**, 640–646 (2003).
56. Wattjes, MPÀ, R. *et al.* Evidence-based guidelines: MAGNIMS consensus guidelines on the use of MRI in multiple sclerosis--establishing disease prognosis and monitoring patients. *Nat. Rev. Neurol.* **11**, 597–606 (2015).
57. Rovira, À. *et al.* Evidence-based guidelines: MAGNIMS consensus guidelines on the use of MRI in multiple sclerosis-clinical implementation in the diagnostic process. *Nat. Rev. Neurol.* **11**, 471–482 (2015).
58. Vattoth, S., Kadam, G. H. & Gaddikeri, S. Revised McDonald Criteria, MAGNIMS Consensus and Other Relevant Guidelines for Diagnosis and Follow Up of MS: What Radiologists Need to Know? *Current Problems in Diagnostic Radiology* vol. 50 389–400 (2021).
59. De Stefano, N. & Filippi, M. MR spectroscopy in multiple sclerosis. *J. Neuroimaging* **17 Suppl 1**, (2007).
60. Swanberg, K. M., Landheer, K., Pitt, D. & Juchem, C. Quantifying the Metabolic Signature of Multiple Sclerosis by in vivo Proton Magnetic Resonance Spectroscopy: Current Challenges and Future Outlook in the Translation From Proton Signal to Diagnostic Biomarker. *Front. Neurol.* **10**, (2019).
61. Fisniku, L. K. *et al.* Disability and T2 MRI lesions: A 20-year follow-up of patients with relapse onset of multiple sclerosis. *Brain* **131**, 808–817 (2008).
62. Button, T. *et al.* Magnetization transfer imaging in multiple sclerosis treated with alemtuzumab. *Mult. Scler.* **19**, 241–244 (2013).
63. Le Page, E. *et al.* Oral versus intravenous high-dose methylprednisolone for treatment of relapses in patients with multiple sclerosis (COPOUSEP): a randomised, controlled, double-blind, non-inferiority trial. *Lancet (London, England)* **386**, 974–981 (2015).
64. Soliven, B., Miron, V. & Chun, J. The neurobiology of sphingosine 1-phosphate signaling and sphingosine 1-phosphate receptor modulators. *Neurology* **76**, (2011).
65. Mehling, M., Johnson, T., Antel, J., Kappos, L. & Bar-Or, A. Clinical immunology of the sphingosine 1-phosphate receptor modulator fingolimod (FTY720) in multiple sclerosis. *Neurology* **76**, (2011).
66. Anthony, D. C., Sibson, N. R., Losey, P., Meier, D. P. & Leppert, D. Investigation of immune and CNS-mediated effects of fingolimod in the focal delayed-type hypersensitivity multiple sclerosis model. *Neuropharmacology* **79**, 534–541 (2014).
67. Balatoni, B. *et al.* FTY720 sustains and restores neuronal function in the DA rat model of MOG-induced experimental autoimmune encephalomyelitis. *Brain Res. Bull.* **74**, 307–316 (2007).
68. Miron, V. *et al.* Fingolimod (FTY720) enhances remyelination following demyelination of organotypic cerebellar slices. *Am. J. Pathol.* **176**, 2682–2694 (2010).
69. Kappos, L. *et al.* A placebo-controlled trial of oral fingolimod in relapsing multiple sclerosis. *N. Engl. J. Med.* **362**, 387–401 (2010).
70. Gajofatto, A. & Benedetti, M. Treatment strategies for multiple sclerosis: When to start, when to change, when to stop? *World J. Clin. cases* **3**, 545 (2015).
71. 't Hart, B. Why does multiple sclerosis only affect human primates? *Mult. Scler.* **22**, 559–563 (2016).
72. Constantinescu, C., Farooqi, N., O'Brien, K. & Gran, B. Experimental autoimmune

encephalomyelitis (EAE) as a model for multiple sclerosis (MS). *Br. J. Pharmacol.* **164**, 1079–1106 (2011).
73. Rivers, T., Sprunt, D. & Berry, G. Observations on Attempts to Produce Acute Disseminated Encephalomyelitis in Monkeys. *J. Exp. Med.* **58**, 39–52 (1933).
74. Freund, J., Stern, E. & Pisani, T. Isoallergic encephalomyelitis and radiculitis in guinea pigs after one injection of brain and Mycobacteria in water-in-oil emulsion. *J. Immunol.* 179–194 (1947).
75. Herz, J., Zipp, F. & Siffrin, V. Neurodegeneration in autoimmune CNS inflammation. *Exp. Neurol.* **225**, 9–17 (2010).
76. Bjelobaba, I., Begovic-Kupresanin, V., Pekovic, S. & Lavrnja, I. Animal models of multiple sclerosis: Focus on experimental autoimmune encephalomyelitis. *J. Neurosci. Res.* **96**, 1021–1042 (2018).
77. Tsunoda, I. & Fujinami, R. Neuropathogenesis of Theiler's murine encephalomyelitis virus infection, an animal model for multiple sclerosis. *J. Neuroimmune Pharmacol.* **5**, 355–369 (2010).
78. Praet, J., Guglielmetti, C., Bernemann, Z., Van Der Linden, A. & Ponsaerts, P. Cellular and molecular neuropathology of the cuprizone mouse model: clinical relevance for multiple sclerosis. *Neurosci. Biobehav. Rev.* **47**, 485–505 (2014).
79. Guglielmetti, C. *et al.* Hyperpolarized 13C MR metabolic imaging can detect neuroinflammation in vivo in a multiple sclerosis murine model. *Proc. Natl. Acad. Sci. U. S. A.* **114**, E6982–E6991 (2017).
80. Matyszak, M. & Perry, V. Demyelination in the central nervous system following a delayed-type hypersensitivity response to bacillus Calmette-Guérin. *Neuroscience* **64**, 967–977 (1995).
81. Matyszak, M., Townsend, M. & Perry, V. Ultrastructural studies of an immune-mediated inflammatory response in the CNS parenchyma directed against a non-CNS antigen. *Neuroscience* **78**, 549–560 (1997).
82. Broom, K. *et al.* MRI reveals that early changes in cerebral blood volume precede blood-brain barrier breakdown and overt pathology in MS-like lesions in rat brain. *J. Cereb. Blood Flow Metab.* **25**, 204–216 (2005).
83. Newman, T. *et al.* T-cell- and macrophage-mediated axon damage in the absence of a CNS-specific immune response: involvement of metalloproteinases. *Brain* **124**, 2203–2214 (2001).
84. Fisher, K. R. *Metabolism in Cerebral Tumors using Hyperpolarized [1-13C]Ethyl Pyruvate*. (2014).
85. Park, I. *et al.* Hyperpolarized 13C magnetic resonance metabolic imaging: application to brain tumors. *Neuro. Oncol.* **12**, 133–144 (2010).
86. Xu, Y. *et al.* Hyperpolarized 13C Magnetic Resonance Imaging Can Detect Metabolic Changes Characteristic of Penumbra in Ischemic Stroke. *Tomogr. (Ann Arbor, Mich.)* **3**, 67–73 (2017).
87. DeVience, S. *et al.* Metabolic imaging of energy metabolism in traumatic brain injury using hyperpolarized [1- 13 C]pyruvate. *Sci. Rep.* **7**, (2017).
88. Bigatello, L. & Pesenti, A. Respiratory Physiology for the Anesthesiologist. *Anesthesiology* **130**, 1064–1077 (2019).
89. Hoffman, W., Albrecht, R. & Miletich, D. Cerebrovascular response to hypoxia in young vs aged rats. *Stroke* **15**, 129–133 (1984).
90. Lu, J. *et al.* Characterization of cerebrovascular responses to hyperoxia and hypercapnia using MRI in rat. *Neuroimage* **45**, 1126–1134 (2009).
91. Floyd, T. *et al.* Independent cerebral vasoconstrictive effects of hyperoxia and accompanying arterial hypocapnia at 1 ATA. *J. Appl. Physiol.* **95**, 2453–2461 (2003).
92. Vestergaard, M. *et al.* Acute hypoxia increases the cerebral metabolic rate - a magnetic resonance imaging study. *J. Cereb. Blood Flow Metab.* **36**, 1046–1058 (2016).
93. Bulte, D., Chiarelli, P., Wise, R. & Jezzard, P. Cerebral perfusion response to hyperoxia. *J. Cereb. Blood Flow Metab.* **27**, 69–75 (2007).
94. Grubb, R., Raichle, M., Eichling, J. & Ter-Pogossian, M. The effects of changes in PaCO2

on cerebral blood volume, blood flow, and vascular mean transit time. *Stroke* **5**, 630–639 (1974).
95. Terraneo, L. & Samaja, M. Comparative Response of Brain to Chronic Hypoxia and Hyperoxia. *Int. J. Mol. Sci.* **18**, (2017).
96. Demchenko, I., Oury, T., Crapo, J. & Piantadosi, C. Regulation of the brain's vascular responses to oxygen. *Circ. Res.* **91**, 1031–1037 (2002).
97. Xu, F., Liu, P., Pascual, J., Xiao, G. & Lu, H. Effect of hypoxia and hyperoxia on cerebral blood flow, blood oxygenation, and oxidative metabolism. *J. Cereb. Blood Flow Metab.* **32**, 1909–1918 (2012).
98. Xu, F., Ge, Y. & Lu, H. Noninvasive quantification of whole-brain cerebral metabolic rate of oxygen (CMRO2) by MRI. *Magn. Reson. Med.* **62**, 141–148 (2009).
99. Noseworthy, M. D. & Bray, T. M. Effect of oxidative stress on brain damage detected by MRI and in vivo 31P-NMR. *Free Radic. Biol. Med.* **24**, 942–951 (1998).
100. Ciarlone, G. & Dean, J. Normobaric hyperoxia stimulates superoxide and nitric oxide production in the caudal solitary complex of rat brain slices. *Am. J. Physiol. Cell Physiol.* **311**, C1014–C1026 (2016).
101. Brutus, N., Hanley, S., Ashraf, Q., Mishra, O. & Delivoria-Papadopoulos, M. Effect of hyperoxia on serine phosphorylation of apoptotic proteins in mitochondrial membranes of the cerebral cortex of newborn piglets. *Neurochem. Res.* **34**, 1219–1225 (2009).
102. Mudduluru, M., Zubrow, A., Ashraf, Q., Delivoria-Papadopoulos, M. & Mishra, O. Tyrosine phosphorylation of apoptotic proteins during hyperoxia in mitochondria of the cerebral cortex of newborn piglets. *Neurochem. Res.* **35**, 1003–1009 (2010).
103. Terraneo, L. *et al.* Brain adaptation to hypoxia and hyperoxia in mice. *Redox Biol.* **11**, 12–20 (2017).
104. Ottolenghi, S., Sabbatini, G., Brizzolari, A., Samaja, M. & Chiumello, D. Hyperoxia and oxidative stress in anesthesia and critical care medicine. *Minerva Anestesiol.* **86**, 64–75 (2020).
105. Baughman, V., Hoffman, W., Miletich, D. & Albrecht, R. Cerebrovascular and cerebral metabolic effects of N2O in unrestrained rats. *Anesthesiology* **73**, 269–272 (1990).
106. Algotsson, L., Messeter, K., Rosén, I. & Holmin, T. Effects of nitrous oxide on cerebral haemodynamics and metabolism during isoflurane anaesthesia in man. *Acta Anaesthesiol. Scand.* **36**, 46–52 (1992).
107. Wu, O. *et al.* Tracer arrival timing-insensitive technique for estimating flow in MR perfusion-weighted imaging using singular value decomposition with a block-circulant deconvolution matrix. *Magn. Reson. Med.* **50**, 164–174 (2003).
108. Eng, J. Sample size estimation: how many individuals should be studied? *Radiology* **227**, 309–313 (2003).
109. Bélanger, M., Allaman, I. & Magistretti, P. J. Brain energy metabolism: Focus on Astrocyte-neuron metabolic cooperation. *Cell Metabolism* vol. 14 724–738 (2011).
110. Prichard, J. *et al.* Lactate rise detected by 1H NMR in human visual cortex during physiologic stimulation. *Proc. Natl. Acad. Sci. U. S. A.* **88**, 5829–5831 (1991).
111. Grist, J. T. *et al.* Quantifying normal human brain metabolism using hyperpolarized [1– 13 C]pyruvate and magnetic resonance imaging. *Neuroimage* **189**, 171–179 (2019).
112. O'Neill, L., Kishton, R. & Rathmell, J. A guide to immunometabolism for immunologists. *Nat. Rev. Immunol.* **16**, 553–565 (2016).
113. Cao, Y., Rathmell, J. & Macintyre, A. Metabolic reprogramming towards aerobic glycolysis correlates with greater proliferative ability and resistance to metabolic inhibition in CD8 versus CD4 T cells. *PLoS One* **9**, (2014).
114. Can, E. *et al.* Noninvasive rapid detection of metabolic adaptation in activated human T lymphocytes by hyperpolarized 13C magnetic resonance. *Sci. Rep.* **10**, (2020).
115. Magistretti, P., Pellerin, L., Rothman, D. & Shulman, R. Energy on demand. *Science* **283**, 496–497 (1999).
116. Orihuela, R., McPherson, C. & Harry, G. Microglial M1/M2 polarization and metabolic states. *Br. J. Pharmacol.* **173**, 649–665 (2016).
117. Tannahill, G., Iraci, N., Gaude, E., Frezza, C. & Pluchino, S. Metabolic reprograming of

mononuclear phagocytes in progressive multiple sclerosis. *Front. Immunol.* **6**, (2015).
118. Galván-Peña, S. & O'Neill, L. Metabolic reprograming in macrophage polarization. *Front. Immunol.* **5**, (2014).
119. Chang, C. & Pearce, E. Emerging concepts of T cell metabolism as a target of immunotherapy. *Nat. Immunol.* **17**, 364–368 (2016).
120. Pearce, E. & Pearce, E. Metabolic pathways in immune cell activation and quiescence. *Immunity* **38**, 633–643 (2013).
121. Angelin, A. *et al.* Foxp3 Reprograms T Cell Metabolism to Function in Low-Glucose, High-Lactate Environments. *Cell Metab.* **25**, 1282-1293.e7 (2017).
122. Fünfschilling, U. *et al.* Glycolytic oligodendrocytes maintain myelin and long-term axonal integrity. *Nature* **485**, 517–521 (2012).
123. Magistretti, P. J. & Allaman, I. Lactate in the brain: from metabolic end-product to signalling molecule. *Nat. Rev. Neurosci.* **19**, 235–249 (2018).
124. Yamagata, K. Lactate Supply from Astrocytes to Neurons and its Role in Ischemic Stroke-induced Neurodegeneration. *Neuroscience* **481**, 219–231 (2022).
125. De Stefano, N. *et al.* Axonal damage correlates with disability in patients with relapsing-remitting multiple sclerosis. Results of a longitudinal magnetic resonance spectroscopy study. *Brain* **121 (Pt 8)**, 1469–1477 (1998).
126. MacKenzie, J. *et al.* Detection of inflammatory arthritis by using hyperpolarized 13C-pyruvate with MR imaging and spectroscopy. *Radiology* **259**, 414–420 (2011).
127. Josan, S. *et al.* Assessing inflammatory liver injury in an acute CCl4 model using dynamic 3D metabolic imaging of hyperpolarized [1-(13)C]pyruvate. *NMR Biomed.* **28**, 1671–1677 (2015).
128. Serres, S. *et al.* Comparison of MRI signatures in pattern I and II multiple sclerosis models. *NMR Biomed.* **22**, 1014–1024 (2009).
129. Vanhamme, L., van den Boogaart, A. & Van Huffel, S. Improved method for accurate and efficient quantification of MRS data with use of prior knowledge. *J. Magn. Reson.* **129**, 35–43 (1997).
130. David, O., Kovarik, J. & Schmouder, R. Clinical pharmacokinetics of fingolimod. *Clin. Pharmacokinet.* **51**, 15–28 (2012).
131. Healy, L. & Antel, J. Sphingosine-1-Phosphate Receptors in the Central Nervous and Immune Systems. *Curr. Drug Targets* **17**, 1841–1850 (2016).